

5-19-2023

## Changes in Nascent Chromatin Structure Regulate Activation of the Pro-fibrotic Transcriptome and Myofibroblast Emergence in Organ Fibrosis

Morgan D. Basta

Svetlana Petruk


Ross Summer

Joel Rosenbloom

Peter J. Wermuth

*See next page for additional authors*

Follow this and additional works at: <https://jdc.jefferson.edu/bmpfp>

 Part of the [Dermatology Commons](#), [Medical Biochemistry Commons](#), [Medical Molecular Biology Commons](#), and the [Medical Pathology Commons](#)

**[Let us know how access to this document benefits you](#)**

This Article is brought to you for free and open access by the Jefferson Digital Commons. The Jefferson Digital Commons is a service of Thomas Jefferson University's [Center for Teaching and Learning \(CTL\)](#). The Commons is a showcase for Jefferson books and journals, peer-reviewed scholarly publications, unique historical collections from the University archives, and teaching tools. The Jefferson Digital Commons allows researchers and interested readers anywhere in the world to learn about and keep up to date with Jefferson scholarship. This article has been accepted for inclusion in Department of Biochemistry and Molecular Biology Faculty Papers by an authorized administrator of the Jefferson Digital Commons. For more information, please contact: [JeffersonDigitalCommons@jefferson.edu](mailto:JeffersonDigitalCommons@jefferson.edu).

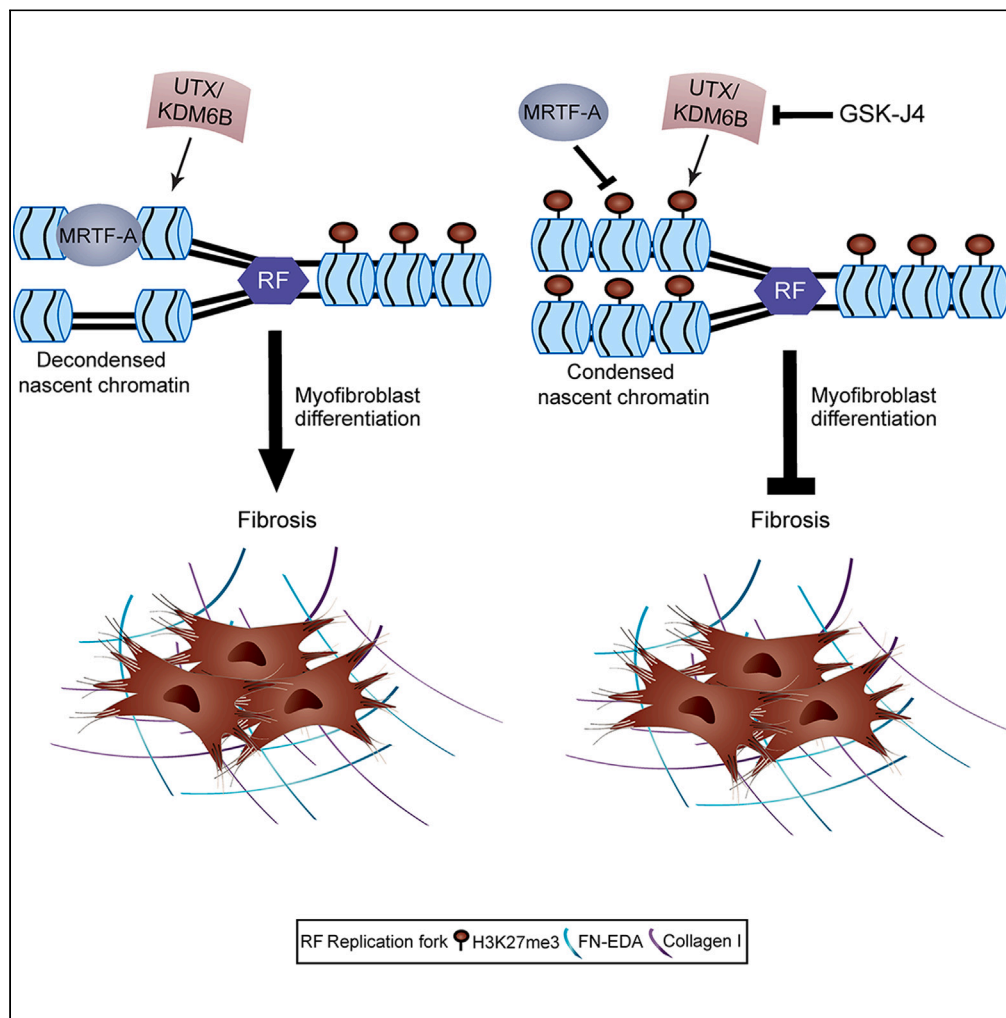
---

**Authors**

Morgan D. Basta, Svetlana Petruk, Ross Summer, Joel Rosenbloom, Peter J. Wermuth, Edward J. Macarak, Alex V. Levin, Alexander Mazo, and Janice L. Walker

## Article

## Changes in nascent chromatin structure regulate activation of the pro-fibrotic transcriptome and myofibroblast emergence in organ fibrosis



Morgan D. Basta,  
Svetlana Petruk,  
Ross Summer, ...,  
Alex V. Levin,  
Alexander Mazo,  
Janice L. Walker

alexander.mazo@jefferson.  
edu (A.M.)  
janice.walker@jefferson.edu  
(J.L.W.)

**Highlights**

UTX/KDM6B  
decondenses nascent  
chromatin structure for  
myofibroblast  
differentiation

Inhibiting UTX/KDM6B  
condenses chromatin to  
block fibrotic  
transcriptome activation

UTX/KDM6B inhibition  
blocks myofibroblast  
emergence and fibrotic  
extracellular matrix (ECM)  
production

Targeting UTX/KDM6B  
has potential therapeutic  
application in lens and  
lung fibrosis

Basta et al., iScience 26,  
106570  
May 19, 2023 © 2023 The  
Author(s).  
[https://doi.org/10.1016/  
j.isci.2023.106570](https://doi.org/10.1016/j.isci.2023.106570)

## Article

## Changes in nascent chromatin structure regulate activation of the pro-fibrotic transcriptome and myofibroblast emergence in organ fibrosis

Morgan D. Basta,<sup>1,8</sup> Svetlana Petruk,<sup>3,8</sup> Ross Summer,<sup>4</sup> Joel Rosenbloom,<sup>5</sup> Peter J. Wermuth,<sup>5</sup> Edward Macarak,<sup>5</sup> Alex V. Levin,<sup>6,7</sup> Alexander Mazo,<sup>3,9,\*</sup> and Janice L. Walker<sup>1,2,9,10,\*</sup>

## SUMMARY

**Cell reprogramming to a myofibroblast responsible for the pathological accumulation of extracellular matrix is fundamental to the onset of fibrosis. Here, we explored how condensed chromatin structure marked by H3K72me3 becomes modified to allow for activation of repressed genes to drive emergence of myofibroblasts. In the early stages of myofibroblast precursor cell differentiation, we discovered that H3K27me3 demethylase enzymes UTX/KDM6B creates a delay in the accumulation of H3K27me3 on nascent DNA revealing a period of decondensed chromatin structure. This period of decondensed nascent chromatin structure allows for binding of pro-fibrotic transcription factor, Myocardin-related transcription factor A (MRTF-A) to nascent DNA. Inhibition of UTX/KDM6B enzymatic activity condenses chromatin structure, prevents MRTF-A binding, blocks activation of the pro-fibrotic transcriptome, and results in an inhibition of fibrosis in lens and lung fibrosis models. Our work reveals UTX/KDM6B as central coordinators of fibrosis, highlighting the potential to target its demethylase activity to prevent organ fibrosis.**

## INTRODUCTION

Fibrosis or scarring can affect nearly all tissues of the body,<sup>1–3</sup> and it is the result of a pathological accumulation of extracellular matrix (ECM), leading to a disruption in tissue architecture and critical organ functions. The major cellular culprit of organ fibrosis is the myofibroblast that expresses alpha smooth muscle actin ( $\alpha$ SMA) and whose dysregulation and continued persistence is largely responsible for excess ECM production, such as collagen I.<sup>4–6</sup> While the origin of myofibroblasts is varied and site-specific,<sup>4,6–8</sup> there are essential features of myofibroblast differentiation regardless of precursor cell type. Over many decades, it has become abundantly clear that transforming growth factor  $\beta$  (TGF $\beta$ ) is a central regulator of myofibroblast formation.<sup>9–11</sup> In conjunction with TGF $\beta$  activity, the mechanical microenvironment is key in driving myofibroblast emergence through changes in tissue stiffness.<sup>12–14</sup> Changes in stiffness of the microenvironment can be communicated through integrin cell surface receptors linked to intracellular mechanosensing focal adhesion proteins to impact the actomyosin cytoskeleton.<sup>13</sup> Changes in the actin cytoskeleton can trigger release of myocardin-related transcription factor A (MRTF-A) to allow for translocation of MRTF-A to the nucleus to drive expression of fibrotic genes.<sup>13–15</sup> Despite our increasing knowledge of the fundamental features of organ fibrosis, we have an incomplete understanding of the molecular mechanism for how precursor cells reprogram to  $\alpha$ SMA-expressing myofibroblasts responsible for fibrosis.

Regardless of tissue origin, all reprogramming of a precursor cell to a myofibroblast cell type requires the adoption of a new transcriptional program. This depends on binding of pro-fibrotic TFs, such as MRTF-A, to DNA for the activation of repressed genes.<sup>9,10,12,15</sup> It is well-established that the regulatory regions of all repressed genes have the most condensed arrays of nucleosomes in the genome, which contain histone H3 tri-methylated at Lys-27 (H3K27me3).<sup>16–19</sup> This condensed structure of nucleosomes creates a barrier for the binding of TFs, and there remains no molecular explanation for how pro-fibrotic TFs overcome condensed chromatin barriers to activate repressed genes and allow for precursor cell reprogramming to a myofibroblast to occur. DNA replication may create a window of opportunity for transient changes in chromatin accessibility on repressed genes because nucleosomes are disassembled at the replication fork and immediately re-assembled behind the fork.<sup>20–22</sup> Importantly, transient changes in chromatin

<sup>1</sup>Department of Pathology and Genomic Medicine, Sidney Kimmel Medical College, Thomas Jefferson University, Philadelphia, PA 19107, USA

<sup>2</sup>Department of Ophthalmology, Sidney Kimmel Medical College, Thomas Jefferson University, Philadelphia, PA 19107, USA

<sup>3</sup>Department of Biochemistry and Molecular Biology, Sidney Kimmel Medical College, Kimmel Cancer Center, Thomas Jefferson University, Philadelphia, PA 19107, USA

<sup>4</sup>Center for Translational Medicine, The Jane and Leonard Korman Respiratory Institute at the Sidney Kimmel Medical College, Thomas Jefferson University, Philadelphia, PA 19107, USA

<sup>5</sup>Department of Dermatology and Cutaneous Biology, The Joan and Joel Rosenbloom Research Center for Fibrotic Diseases, Sidney Kimmel Medical College Thomas Jefferson University, Philadelphia, PA 19107, USA

<sup>6</sup>Wills Eye Hospital, Philadelphia, PA 19107, USA

<sup>7</sup>Present address: Flaum Eye Institute and Golisano Children's Hospital, University of Rochester, Rochester, NY 14534, USA

<sup>8</sup>These authors contributed equally

<sup>9</sup>Senior author

<sup>10</sup>Lead contact

\*Correspondence: alexander.mazo@jefferson.edu (A.M.), janice.walker@jefferson.edu (J.L.W.)

<https://doi.org/10.1016/j.isci.2023.106570>



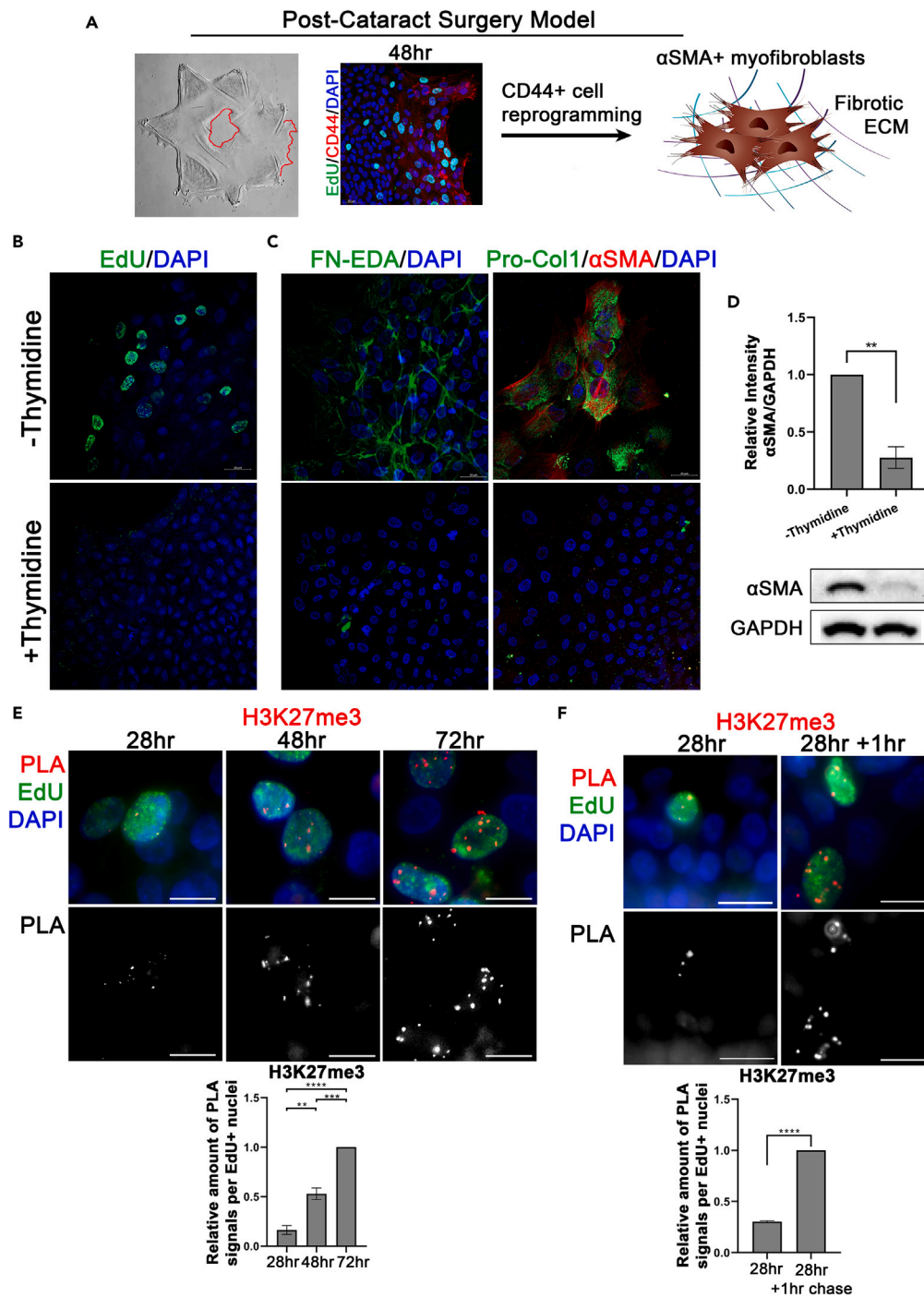


**Figure 1. DNA replication is required for transition of CD44<sup>+</sup> precursor cells to a fibrotic phenotype and H3K27me3 recruitment to nascent DNA is delayed in highly replicative CD44<sup>+</sup> precursor cells**

(A) Mock cataract surgery on isolated lenses produces a star-shaped explant. In response to mock cataract surgery wounding, proliferating (Edu, green) CD44<sup>+</sup> leader cells (red) migrate to sites of injury (leader cells marked by red lines) as well as serve as  $\alpha$ SMA<sup>+</sup> myofibroblast progenitor cells.<sup>28,29</sup>

(B–D) Post-cataract surgery *ex vivo* lens explants were treated with +/- thymidine on day 1 – day 3 post-injury. (B) Representative images of 30min Edu incorporation in DNA of leader cells. Cultures were counterstained with DAPI (4',6'-diamidino-2-phenylindole) (blue). (C) Representative confocal immunofluorescence images of FN-EDA (green) or Pro-Collagen I (green),  $\alpha$ SMA (red) and cultures were counterstained with DAPI (blue). (D) Representative immunoblots

### Figure 1. Continued

of  $\alpha$ SMA and GAPDH (loading control) with graph depicting relative intensity of  $\alpha$ SMA/GAPDH. (E) Representative CAA images of H3K27me3 (red) recruitment to 30min EdU-labeled DNA (green) in nuclei (blue) of leading-edge cells at 28h, 48h, and 72h post-injury. PLA is shown in red and in split channel (black and white). Graph depicts relative amount of PLA per EdU labeled nuclei. Scale bar: 10 $\mu$ m.

(F) Representative CAA images of H3K27me3 (red) recruitment to 30min EdU-labeled DNA (green) in nuclei (blue) of leading-edge cells at 28h and 28h + 1h chase post-injury. PLA is shown in red and in split channel (black and white). Graph depicts relative amount of PLA per EdU labeled nuclei. Scale bar: 10  $\mu$ m. Data are expressed as average  $\pm$  SEM of three independent experiments (D–F). Data is relative to GAPDH and normalized to control (-thymidine) (D).

Data is normalized to 72h (E) and 28h + 1h (F). \*\*p < 0.01, \*\*\*p < 0.001, \*\*\*\*p < 0.0001 by one-way ANOVA (E) or unpaired t-test (D and F). Scale bar: 20 $\mu$ m (A–C).

accessibility just after DNA replication were shown to facilitate TF binding and alterations in gene expression, leading to cell differentiation.<sup>20,23,24</sup>

H3K27 methylation and chromatin structure is regulated by the interplay of the opposing H3K27-specific histone modifying enzymes. Ubiquitously transcribed tetratricopeptide repeat, X (UTX), the major H3K27me3 demethylase (KDM), and Lysine demethylase 6B (KDM6B) are responsible for demethylating H3K27 to induce a more decondensed structure of chromatin amenable to TF binding. Whereas, enhancer of zeste homolog 2 (EZH2) is a histone methyltransferase (HMT) enzyme that is primarily responsible for trimethylating H3K27 to create a condensed structure of chromatin which creates a barrier to TF binding.<sup>25</sup> Here, we investigated whether DNA replication may present the opportunity for the association of UTX/KDM6B to oppose EZH2 HMT activity on repressed genes leading to a decondensed structure of chromatin to allow for binding of pro-fibrotic TFs with DNA to activate an array of pivotal genes associated with the myofibroblast phenotype. Using the lens as our primary model of organ fibrosis along with classic *in-vitro* and *in-vivo* models of lung fibrosis, we explored this hypothesis to expand our molecular understanding of how precursor cells reprogram to disease-causing myofibroblasts and to uncover a potential new therapeutic target for the prevention of fibrosis.

## RESULTS

### DNA replication is necessary for CD44<sup>+</sup> precursor cell reprogramming to an $\alpha$ SMA-expressing myofibroblast and fibrotic matrix production

To explore the molecular underpinnings of precursor cell reprogramming to a myofibroblast we used our previously developed *ex vivo* post-cataract surgery chicken lens model which recapitulates the major features of the lens fibrotic disease, posterior capsule opacification (PCO).<sup>26,27</sup> In the *ex vivo* post-cataract surgery lens model proliferating CD44<sup>+</sup> leader cells serve as a source for myofibroblast precursor cells<sup>28,29</sup> and transition to  $\alpha$ SMA-expressing myofibroblasts on day 3 post-injury<sup>29</sup> (Figure 1A, model). Previously, we have shown that the CD44<sup>+</sup> derived  $\alpha$ SMA-expressing myofibroblasts are the main producers of the fibrotic ECM proteins, fibronectin extra domain A splice variant (FN-EDA) and type I collagen (Figure 1A, model).<sup>30</sup> Since cell division is essential for most cell reprogramming,<sup>21,31</sup> we determined if DNA replication is necessary to drive CD44<sup>+</sup> precursor cell transition to a myofibroblast and production of fibrotic ECM. To test this, we used thymidine from 24h to 72h post-injury to arrest cells in the S-phase of the cell cycle and to determine what effect this would have on myofibroblast emergence and the fibrotic phenotype at 72h post-injury. Thymidine treatment successfully inhibited leader cells from undergoing replication as evidenced by the block in EdU incorporation (Figure 1B). Preventing leader cells from undergoing replication blocked production of major fibrotic ECM proteins, FN-EDA and pro-collagen I (Figure 1C). Furthermore, thymidine treatment prevented the emergence of  $\alpha$ SMA-expressing myofibroblasts (Figure 1C, D, p = 0.0016), confirming a key role for DNA replication in regulating the developing fibrotic phenotype.

### Post-replicative nascent chromatin structure is transiently decondensed in myofibroblast precursor cells

Given the above findings and that nucleosomes are disassembled and then re-assembled at the time of DNA replication, we mapped the state of post-replicative chromatin structure during differentiation of precursor cells into myofibroblasts using the chromatin assembly assay (CAA).<sup>32</sup> The CAA allows for the examination of the recruitment of any protein to the EdU-labeled (post-replicative) DNA *in-situ* in single cells.<sup>32</sup> Since CAA is performed in non-synchronized cells, the results in multiple nuclei reflect firing of all replicons throughout the genome. Using H3K27me3 as a marker for the most condensed arrays of nucleosomes in

the genome<sup>16–19</sup> and using this marker to map the structure of chromatin during cell reprogramming to a myofibroblast (28hr–72h post-injury), we investigated the recruitment of H3K27me3 to nascent DNA in replicating leader cells using CAA. We found minimal accumulation of H3K27me3 on the 30min EdU-labeled nascent DNA at 28h post-injury, while it greatly accumulates at 48h with further increase at 72h post-cataract surgery wounding (Figure 1E) hr vs. 48 h  $P = 0.0021$ , 48h vs. 72 h  $P = 0.0006$ , 28h vs. 72 h  $P < 0.0001$ ). The increase in H3K27me3 recruitment to nascent DNA at 72h coincides with emergence of  $\alpha$ SMA expressing myofibroblasts.<sup>29</sup> The delay in accumulation of H3K27me3 on nascent DNA at 28h and rapid accumulation of H3K27me3 after 48h post-injury demonstrates that the structure of chromatin is transiently decondensed during early transition period of the myofibroblasts precursor cells to  $\alpha$ SMA+ myofibroblasts and that later stages of reprogramming are characterized by condensed structure of post-replicative chromatin structure. To further define the period of the decondensed structure of chromatin after DNA replication at 28h post-injury, we performed 30min EdU-labeling followed with a 1h chase. We observed a significant increase in H3K27me3 accumulation on nascent DNA after chase (Figure 1F,  $p < 0.0001$ ). This suggests that decondensed structure of chromatin is a transient event that occurs for a short period of time after DNA replication. Therefore, our data reveals a potential window of opportunity for cell reprogramming to a myofibroblast to be initiated when nascent chromatin is decondensed at 28h post-injury.

### UTX/KDM6B activity is required to decondense nascent chromatin in myofibroblast precursor cells

Transient delay in accumulation of H3K27me3 on nascent chromatin during the window of decondensed chromatin structure in myofibroblast precursor cells at 28h after injury may be the result of the enhanced activity of the KDM enzymes UTX/KDM6B, or reduced activity of the HMT EZH2, or both. To investigate this, we examined the kinetics of expression and association of UTX, KDM6B, and EZH2 with nascent DNA during the window of decondensed chromatin structure in myofibroblast precursor cells. We found that UTX and KDM6B are localized to the nuclei of both CD44<sup>+</sup> and CD44<sup>−</sup> cells at 28h and 48h post-injury prior to myofibroblast emergence (Figure 2A  $p = 0.294596$ ,  $p = 0.004657$  and Figure 2B  $p = 0.901146$ ,  $p = 0.860609$ ). The H3K27 HMT enzyme, EZH2, is expressed in the nuclei of all cells and with greater intensity within the nuclei of CD44<sup>+</sup> precursor leader cells (Figure 2C  $p = 0.064037$ ,  $p = 0.015347$ ). Given that CAA shows that all enzymes are associated with DNA at 28h post-injury (Figure 2D  $p < 0.0001$ , E  $p = 0.0026$ , F  $p = 0.0105$ ), we speculated that KDM activity of UTX/KDM6B is predominant over the EZH2 HMT activity at this time. To examine this and to determine if UTX/KDM6B KDM activity is responsible for the period of decondensed nascent chromatin structure, we used GSK-J4, a small molecule inhibitor selective for both KDM enzymes UTX and KDM6B.<sup>33</sup> Treatment with GSK-J4 during the window of decondensed chromatin structure at 28h post-injury now allowed for EZH2 HMT activity to lead to a significant increase in accumulation of H3K27me3 to nascent DNA compared to vehicle (DMSO) alone (Figure 2G,  $p = 0.0396$ ). This suggests that UTX/KDM6B demethylases are primarily responsible for low accumulation of H3K27me3 on nascent DNA at 28h post-injury, likely masking EZH2 HMT activity. Thus, our results suggest that UTX/KDM6B are essential for the observed decondensation of nascent chromatin during early stages of myofibroblast differentiation and that pharmacological inhibition of these enzymes cause condensation of the post-replicative chromatin structure in the myofibroblast precursor cells.

### Recruitment of MRTF-A to nascent DNA of the myofibroblast precursor cells is dependent on decondensed structure of post-replicative chromatin

We next aimed to determine whether decondensed nascent chromatin is essential for recruitment of the major pro-fibrotic TF, MRTF-A, to DNA of the myofibroblast precursor cells. By immunofluorescence staining we found that MRTF-A is localized to the nuclei of cells on day 1 post-injury (Figure 3A). Using CAA, we detected robust accumulation of MRTF-A to nascent DNA of the myofibroblast precursor cells at 28h post-injury (Figure 3B), the time when nascent chromatin is decondensed (Figure 1E). We further examined whether decondensed nascent chromatin is essential for recruitment of MRTF-A to DNA. To this end, we inhibited the enzymatic activity of UTX/KDM6B with GSK-J4, which condenses nascent chromatin (Figure 2G). We found that GSK-J4 treatment during the window of decondensed chromatin structure at 28h post-injury prevented recruitment of MRTF-A to nascent DNA of the myofibroblast precursor cells compared to vehicle alone (Figure 3C,  $p = 0.0008$ ). These results suggest that decondensed nascent chromatin structure induced by UTX KDM activity is essential for recruitment of MRTF-A to DNA.

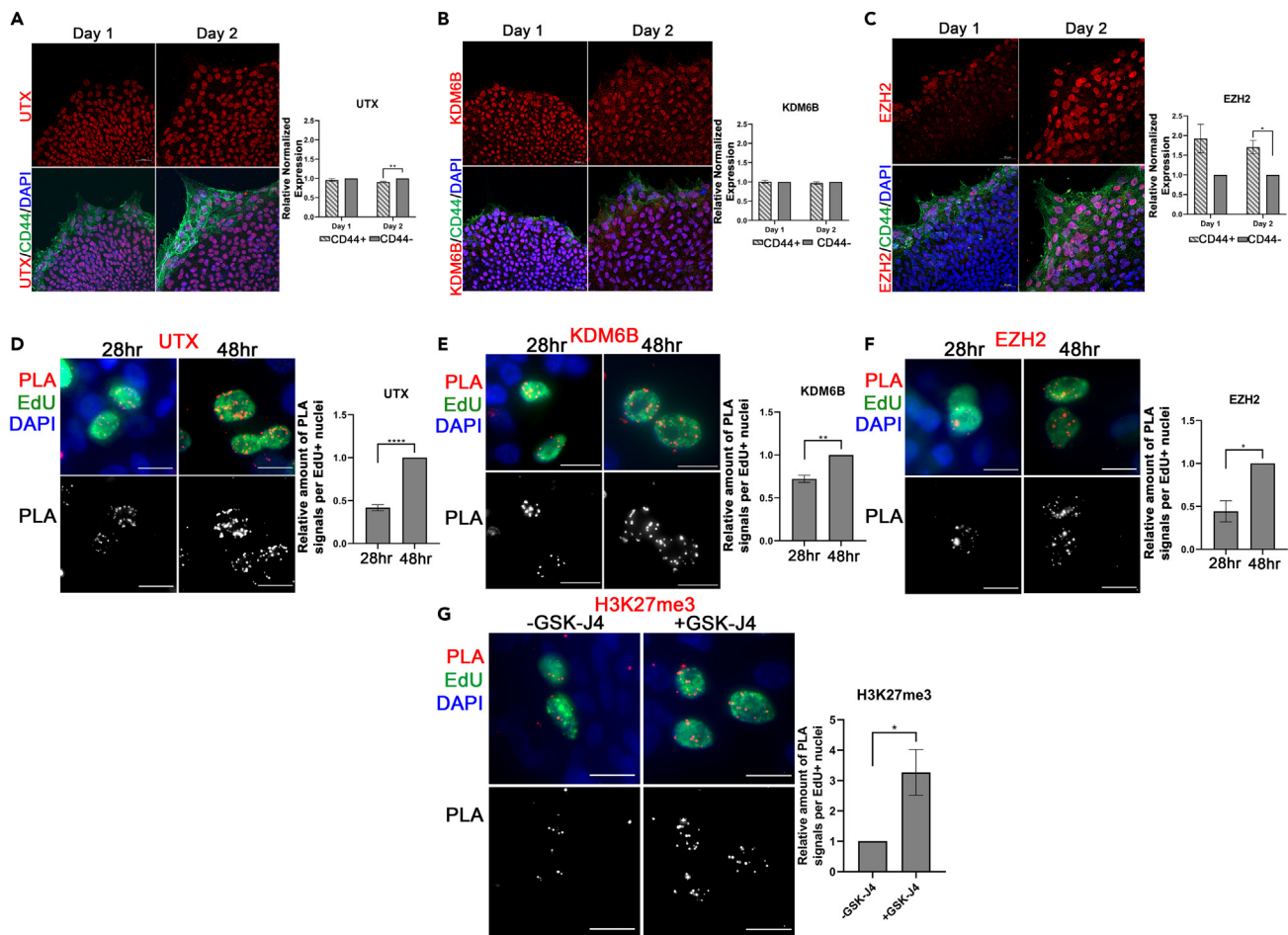


**Figure 2. UTX KDM activity is required to decondense nascent chromatin in myofibroblast precursor cells**

(A–C) Representative confocal immunofluorescence images of UTX, KDM6B, and EZH2 expression (red) within CD44<sup>+</sup> (green) compared to CD44<sup>-</sup> cells on day 1 and day 2 post-injury. Graph depicts relative intensity of UTX, KDM6B, or EZH2 in DAPI labeled nuclei (blue). Scale bar: 20μm. (A) Post-cataract surgery culture labeled for UTX or shown as an overlay for UTX, CD44, and DAPI. (B) Post-cataract surgery culture labeled for KDM6B or shown as an overlay for KDM6B, CD44, and DAPI. (C) Post-cataract surgery culture labeled for EZH2 or shown as an overlay for EZH2, CD44, and DAPI.

(D–F) Representative CAA images of UTX, KDM6B, and EZH2 (red) recruitment to 30min EdU-labeled DNA (green) in nuclei (DAPI) of leading-edge cells at 28h and 48h post-injury. Graphs depict the relative amount of PLA per EdU labeled nuclei. Scale bar: 10μm.

(G) Representative images of H3K27me3 recruitment (red) to 30min EdU-labeled DNA (green) in leader cell nuclei (blue) measured by CAA in the absence (–) and presence (+) of GSK-J4 treatment at 28h post-injury. The graph depicts the relative amount of PLA per EdU labeled nuclei. Scale bar: 10 μm. Data are expressed as average ± SEM of three independent experiments (A–G). Data is normalized to CD44<sup>+</sup> cells (A–C). Data is normalized to 48h (D–F) or control (–GSK-J4) (G). \*p < 0.05, \*\*p < 0.01, \*\*\*\*p < 0.0001 by unpaired t-test (A–G).

Since we have hypothesized that these events are occurring specifically at the time of DNA replication, we then wanted to determine if MRTF-A recruitment to nascent DNA only occurs during S-phase. For these experiments, DNA replication was blocked using thymidine. In control experiments, we confirmed that treatment with thymidine effectively blocked DNA replication and that release of thymidine block for 4h resumed DNA replication (Figure 3D). Blocking DNA replication with thymidine completely inhibited MRTF-A recruitment to nascent DNA (Figure 3E). Thymidine treatment also led to an increase in the global level of H3K27me3 (Figure S1), which is also in line with inhibition of binding of MRTF-A. However, release from thymidine block for 4h to resume DNA synthesis led to abundant association of MRTF-A with nascent DNA (Figure 3E, p = 0.0002). These data provide evidence that MRTF-A is recruited to nascent DNA in myofibroblast precursor cells only during S-phase consistent with our earlier findings that cell reprogramming to a fibrotic phenotype is dependent on DNA replication (Figures 1C–1D).

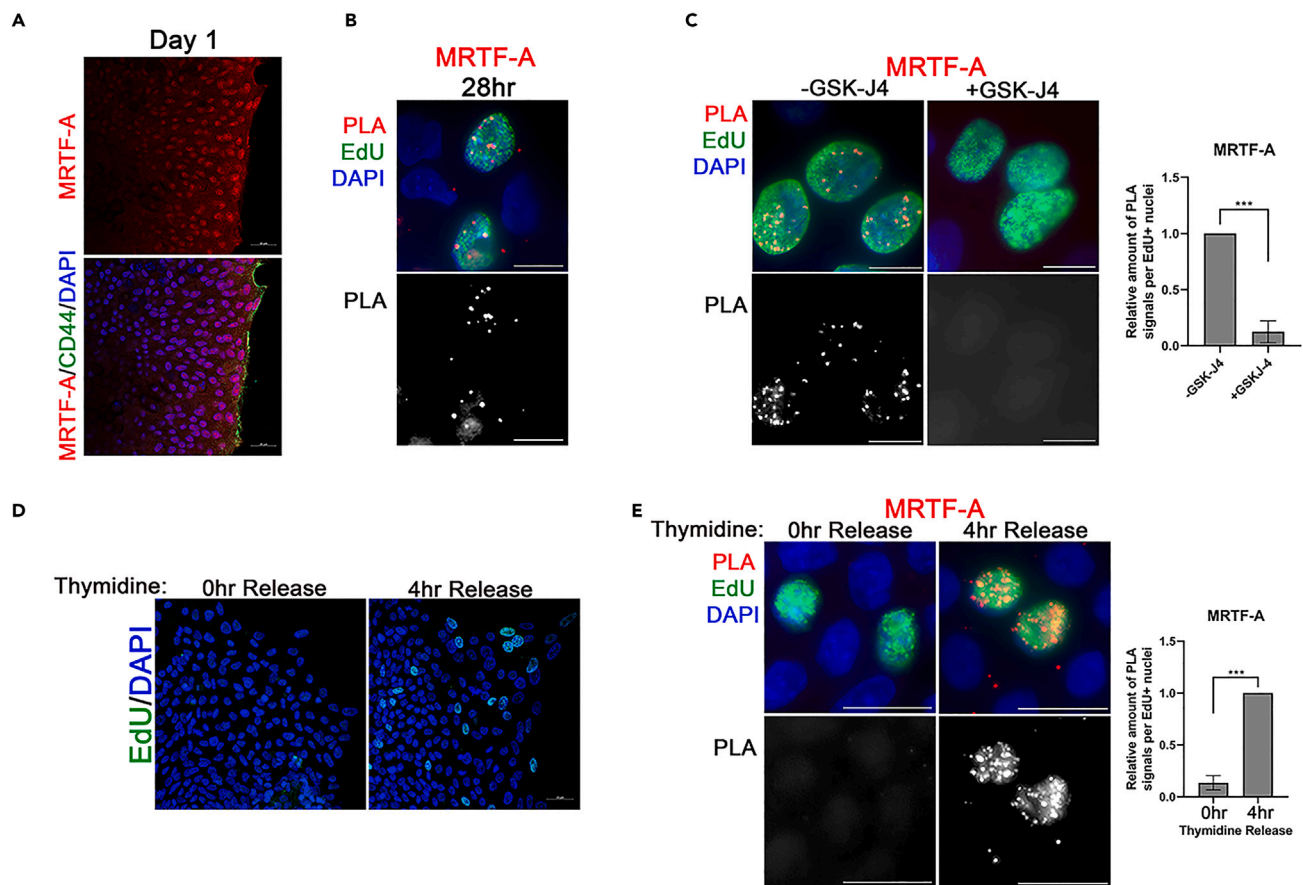


**Figure 3. Recruitment of MRTF-A to nascent DNA of the myofibroblast precursor cells is dependent on decondensed structure of post-replicative chromatin**

(A) Representative confocal immunofluorescence images of MRTF-A (red) localization as well as an overlay of MRTF-A (red), CD44 (green) expression with DAPI counterstain (blue) on day 1 post-injury. Scale bar: 20μm.

(B–C) Representative CAA images of MRTF-A (red) recruitment to 30min EdU-labeled DNA (green) in nuclei (DAPI) at 28h post-injury. PLA is shown in red and in split channel (black and white). Scale bar: 10μm. (C) MRTF-A recruitment to nascent DNA in the absence (–) and presence (+) GSK-J4. Graph depicts relative amount of PLA per EdU labeled nuclei.

(D) Representative images of EdU-incorporation (green) in myofibroblast progenitor cells after cultures were treated in the presence of thymidine for 24h and thymidine block was removed for 0h and 4h. Cultures were counterstained with DAPI (blue). Scale bar: 20μm.

(E) Representative CAA images of MRTF-A (red) in myofibroblast progenitor cells after cultures were treated in the presence of thymidine for 24h and thymidine block was removed for 0h and 4h. Scale bar: 20 μm. Graph depicts relative amount of PLA signals per EdU labeled nuclei. Data are expressed as average ± SEM of three independent experiments (C, E). Data is normalized to -GSK-J4 (C) or 4h thymidine release (E). \*\*\*p < 0.001 by unpaired t-test (C, E).

### Condensing chromatin structure with GSK-J4 leads to downregulation of specific gene sets associated with fibrosis

The above proof-of-concept experiments demonstrating that MRTF-A recruitment to nascent DNA is blocked with inhibition of UTX/KDM6B KDM activity using GSK-J4 suggests there would be an alteration in subsequent gene expression events when chromatin structure is condensed. To assess this, RNA sequencing (RNA-Seq) analysis was performed on day 3 post-cataract surgery lens explants treated with GSK-J4 or vehicle control to discover differentially expressed genes (DEGs) ( $p < 0.05$ , Figure 4). Hierarchical clustering map for differential gene expression from samples treated with GSK-J4 compared to samples treated with vehicle showed distinct clustering between groups (Figure 4A). To explore the impact of condensing chromatin with GSK-J4 on gene repression, we focused our subsequent analyses on the 1,407 significantly downregulated DEGs (Figure 4B,  $p < 0.05$ ). We discovered major fibrosis-related genes such as ACTA2, collagen type I alpha I chain (COL1A1), collagen type I alpha II chain (COL1A2), FN1, and TGFB1, are all downregulated with GSK-J4 treatment (Figure 4B).

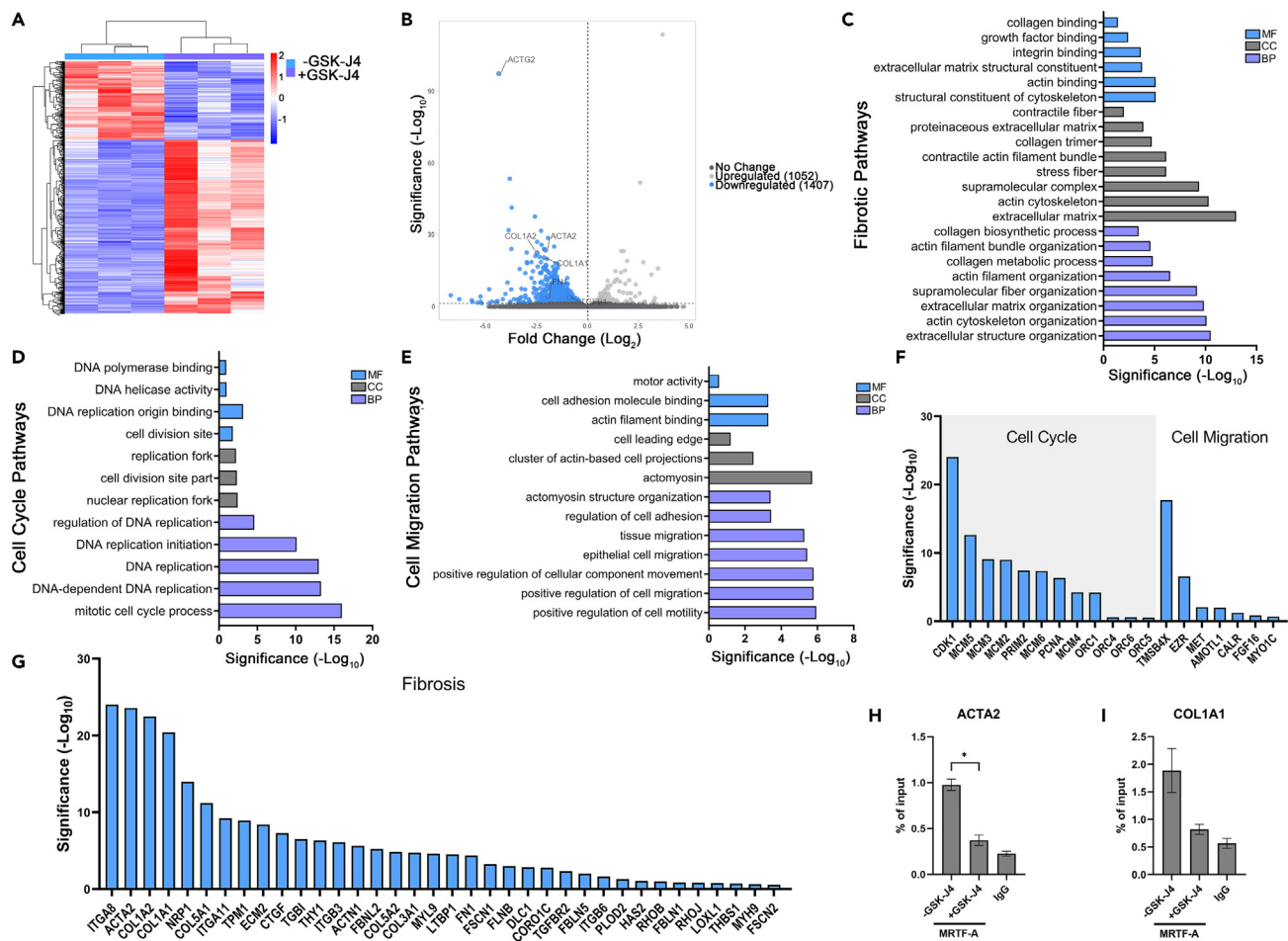


**Figure 4. Condensing chromatin structure with GSK-J4 leads to downregulation of specific gene sets associated with fibrosis**

(A) Hierarchical clustering map of differential expression genes from samples treated with GSK-J4 (+) and vehicle control (-).  
 (B) Volcano plot showing the number of upregulated and downregulated DEGs between -GSK-J4 and +GSK-J4. Representative downregulated DEGs are shown.  
 (C–E) Representative top GO processes of downregulated genes from -GSK-J4 vs. +GSK-J4. (C) Fibrosis-related GO processes.  
 (D) Cell cycle-related GO processes.  
 (E) Cell migration-related GO processes.  
 (F) Representative cell cycle and cell migration-related downregulated DEGs from selected GO processes.  
 (G) Representative fibrosis-related downregulated DEGs from selected GO processes.  
 (H–I) Chromatin was immunoprecipitated with MRTF-A antibody and IgG isotype control +/- GSK-J4. qPCR was performed for MRTF-A-containing genes: ACTA2 and COL1A1. \*p < 0.05 by unpaired t-test (H).

Gene ontology (GO) and Kyoto encyclopedia of genes and genomes (KEGG) independent analyses were performed to determine the biological impact of downregulated DEGs (Figures 4C–4F and S2B). GO analysis revealed that GSK-J4 treatment downregulated major biological processes (BP), cellular components (CC), and molecular functions (MF) associated with fibrosis, including ECM and actin cytoskeleton-related processes (Figure 4C). The major GO MFs downregulated with GSK-J4 are represented in a directed acyclic graph (DAG) to display relationships between MFs (Figure S2A). The narrower functional terms displayed in the DAG show downregulation of structural constituent of the cytoskeleton, ECM structural constituent, actin binding, and integrin binding (Figure S2A). These MFs are all key to driving fibrotic ECM accumulation and the mechanical signaling between the ECM and the cell to drive myofibroblast emergence and fibrosis.

In addition to fibrosis-related processes, GO analysis found that GSK-J4 treatment downregulated major cell cycle processes. These included the mitotic cell cycle, replication fork, and DNA replication origin binding (Figure 4D). This reveals an interesting role for UTX KDM activity in the regulation of DNA replication in

response to injury. GSK-J4 treatment also resulted in a downregulation of migration processes related to wound repair (Figure 4E). Because fibrosis can be the result of an aberrant wound healing process, identifying any implications on normal wound repair is an important finding when considering GSK-J4 as a potential therapeutic. This included the downregulation of positive regulation of cell migration, actomyosin, and cell adhesion molecule binding process (Figure 4E). Independent KEGG analysis revealed downregulated pathways that mirrored the processes identified in GO analysis (Figure S2B) that included genes associated with DNA replication, ECM-receptor interaction, and regulation of actin cytoskeleton (Figure S2B).

Together, these results prompted us to explore the specific DEGs associated with these major GO analysis enrichment gene sets in greater depth. Representative DEGs found to be downregulated with GSK-J4 treatment in addition to the earlier ones discussed are cell cycle related DEGs that include many genes that constitute the minichromosomal maintenance protein complex (MCM) and origin recognition complex (ORC) that are essential for DNA replication<sup>34</sup> (Figure 4F). GSK-J4 treatment also downregulated DEGs associated with cell migration including *TMSB4X*, *MYO1C*, *AMOTL1*, and *CALR* (Figure 4F).

Importantly, we discovered the downregulation of many fibrosis-related DEGs with GSK-J4 treatment including those essential to TGF $\beta$  activation and signaling including *TGFBR2*, *ITGB6*, *ITGB3*, *LTBP1* (Figure 4G). Downregulated DEGs were associated with formation, regulation and signaling from the fibrotic ECM include *CTGF*, *COL5A1*, *COL5A2*, *COL3A1*, *LOXL1*, *PLOD2*, *FBLN1*, *FBLN2*, *FBLN5*, *ITGA8*, *ITGA11* (Figure 4G). Specific DEGs involved in regulating mechanosensitive focal adhesion complexes include *DLC1*, *CORO1C*, *NRP1*, and *THY1* (Figure 4G), and genes associated with the formation and function of the stress fiber contractile machinery of cell include *RHOB*, *ACTN1*, *FSCN1*, *TPM1*, *MYH9*, and *MYL9* (Figure 4G). These genes are essential to create the mechanosensing machinery of the cells to promote fibrosis.<sup>14</sup> As expected, many of the genes affected by GSK-J4 treatment are MRTF-A target genes, such as *COL1A1* and *ACTA2* (Figures 4B and 4G) and many structural and regulatory constituents of the actin cytoskeleton, including *ACTN1*, *FBLN5*, *MYL9*, and *MYH9*. To determine whether MRTF-A binding to pro-fibrotic genes is dependent on decondensed chromatin structure, we inhibited UTX/KDM6B KDM activity with GSK-J4 and performed chromatin immunoprecipitation (ChIP) at 72h. ChIP confirms that the binding of MRTF-A to major pro-fibrotic target genes, *ACTA2* and *COL1A1*, is dependent on a decondensed structure of chromatin (Figure 4H  $p = 0.0187$ , I). However, it is likely that the 1,407 downregulated DEGs by GSK-J4 treatment are not all regulated by MRTF-A. This indicates that condensing chromatin with GSK-J4 can prevent binding of multiple TFs to block the activation of the fibrotic transcriptome. Therefore, we looked at the expression and recruitment to nascent DNA of another mechanosensitive pro-fibrotic TF, Yes-associated protein 1 (YAP), at 28h when chromatin structure is decondensed. These experiments revealed that YAP was localized to the nuclei and recruited to nascent DNA in the CD44<sup>+</sup> myofibroblast progenitor cells (Figure S3). Collectively, other TFs may have important roles alongside MRTF-A in driving activation of the pro-fibrotic transcriptome.

### GSK-J4 prevents establishment of the pro-fibrotic phenotype in lens post-cataract surgery models

Since we discovered that GSK-J4 treatment leads to downregulation of the gene sets associated with fibrosis, we investigated the effect GSK-J4 has on the fibrotic phenotype. First, we confirmed using RT-qPCR that mRNA expression of the two major fibrotic genes,  $\alpha$ SMA (*ACTA2*) ( $p = 0.0067$ ) and *COL1A1* ( $p = 0.0120$ ) were significantly reduced on day 3 following daily GSK-J4 treatment (Figures 5A and 5B). Importantly, daily GSK-J4 treatment blocked the emergence of the  $\alpha$ SMA-expressing myofibroblasts (Figure 5C,  $p < 0.0001$ ; Figure 5D,  $p = 0.0004$ ), deposition of FN-EDA matrix (Figure 5E,  $p < 0.0001$ ), and production of type I pro-collagen (Figure 5F,  $p = 0.0006$ ). We also found that adding GSK-J4 only during the window of decondensed chromatin structure for a 24h period blocked production of type I pro-collagen (Figures S4A, and B  $p = 0.0001$ ) and  $\alpha$ SMA-expressing myofibroblast emergence on day 3 post-injury (Figure S4A; C,  $p = 0.0014$ ; D,  $p = 0.0131$ ). The downregulated cell cycle-related gene sets we discovered in our RNA-seq analysis (Figures 4C and 4G) prompted us to determine whether replication is impacted in leader cells. Indeed, daily GSK-J4 treatment blocked leader cells from undergoing replication on day 3 (Figure 5G,  $p < 0.0001$ ). Altogether, these results demonstrate that treatment with GSK-J4 effectively blocked reprogramming of precursor leader cells to the fibrotic phenotype.

### Therapeutic potential of GSK-J4 for lens fibrosis

We also assessed the effect of GSK-J4 on fibrotic disease development in the clinically relevant<sup>35–37</sup> human lens pediatric post-cataract surgery model.<sup>28</sup> For these studies, we obtained anterior lens capsule tissue

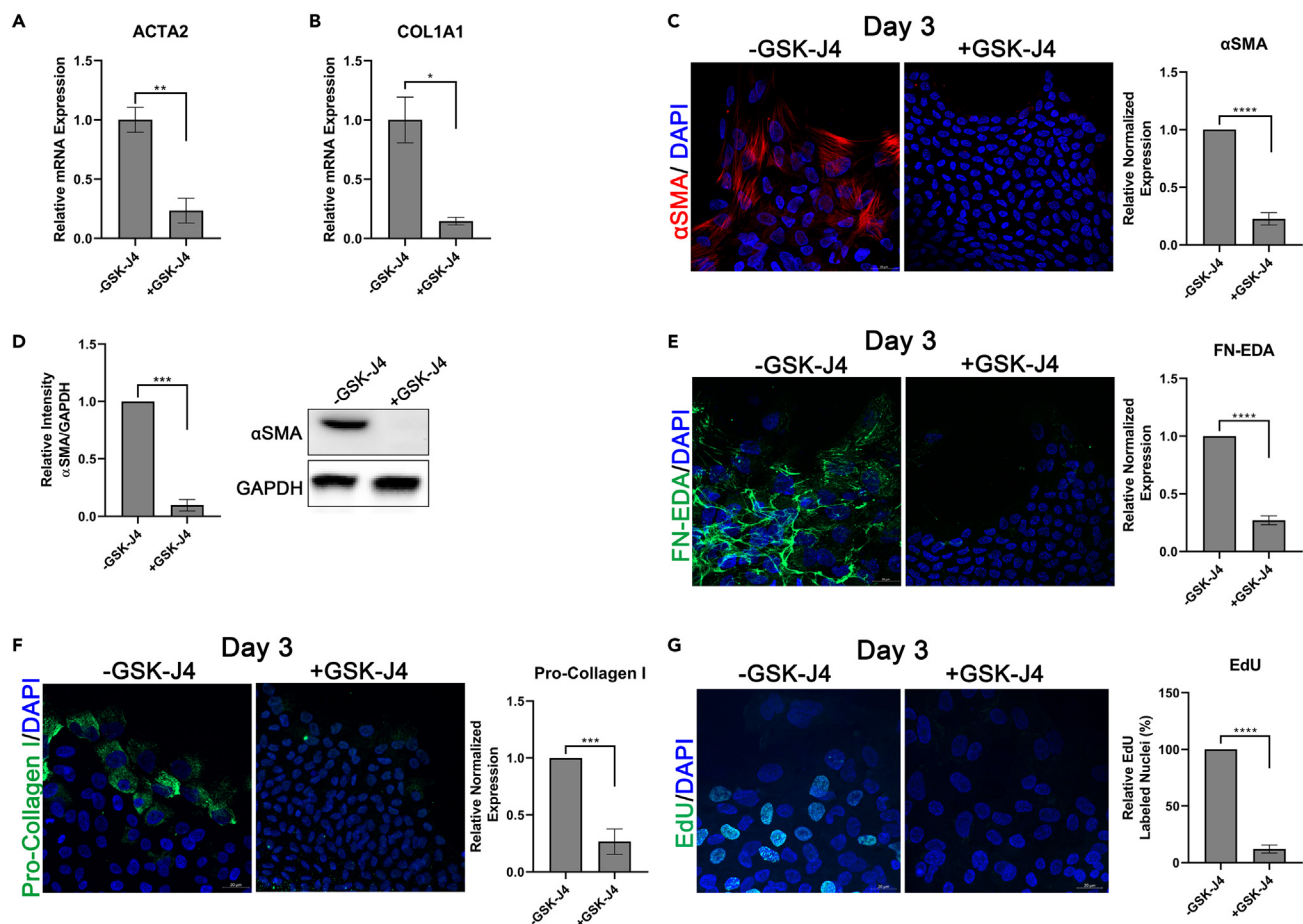


**Figure 5. Condensing chromatin with GSK-J4 prevents cell reprogramming to a pro-fibrotic phenotype in the post-cataract surgery model**

(A–B) Relative gene expression (normalized to *GAPDH*) in the absence (–) and presence (+) of GSK-J4 on day 3 in lens post-cataract surgery cultures. Data is normalized to –GSK-J4 as control.

(A) *ACTA2* ( $\alpha$ SMA) relative gene expression.

(B) *Col1A1* (Collagen I  $\alpha$  I chain) relative gene expression (C, E, F) Representative confocal images of day 3 lens post-cataract surgery cultures treated +/– GSK-J4. Scale bar: 20  $\mu$ m. Graphs depict quantification of fluorescence intensity normalized to control (–GSK-J4).

(C) Post-cataract surgery culture labeled for  $\alpha$ SMA (red) and counterstained for DAPI (blue).

(D) Representative immunoblots (right) for  $\alpha$ SMA and GAPDH (loading control). Graph (left) depicts relative intensity of  $\alpha$ SMA/GAPDH of day 3 +/– GSK-J4 treated lens cultures.

(E) Post-cataract surgery culture labeled for FN-EDA (green) and counterstained for DAPI (blue).

(F) Post-cataract surgery culture labeled for Pro-collagen I (green) and counterstained for DAPI (blue).

(G) Post-cataract surgery culture treated +/– GSK-J4 labeled for 30min EdU (green) and counterstained for DAPI (blue). Graph depicts % of EdU+ cells. Scale bar: 20  $\mu$ m. Data is expressed as average  $\pm$  SEM of at least three independent experiments. Data is normalized to –GSK-J4 (A–G) \* $p$  < 0.05, \*\* $p$  < 0.01, \*\*\* $p$  < 0.001, \*\*\*\* $p$  < 0.0001 by unpaired t-test.

with associated cells from human pediatric cataract surgery patients that were cultured *ex vivo* as explants. Explants were treated with either vehicle or GSK-J4 through day 6, a time when a robust number of  $\alpha$ SMA+ myofibroblasts are usually present. Treatment with GSK-J4 significantly reduced the appearance of  $\alpha$ SMA-expressing myofibroblasts (Figure S4A,  $p=0.0069$ ), corroborating the above findings in the chicken post-cataract surgery model.

The downregulation of cell migration-associated genes discovered in our RNA-analysis (Figures 4E and 4F) suggests that GSK-J4 could impact wound healing. Because our studies highlight GSK-J4 as a potential therapeutic target for the treatment of injury-induced fibrosis, we wanted to determine whether GSK-J4 would impact normal wound healing. The *ex vivo* post-cataract surgery model allows us to study both fibrotic and normal wound repair simultaneously.<sup>29,30,38</sup> To test whether GSK-J4 has any effect on

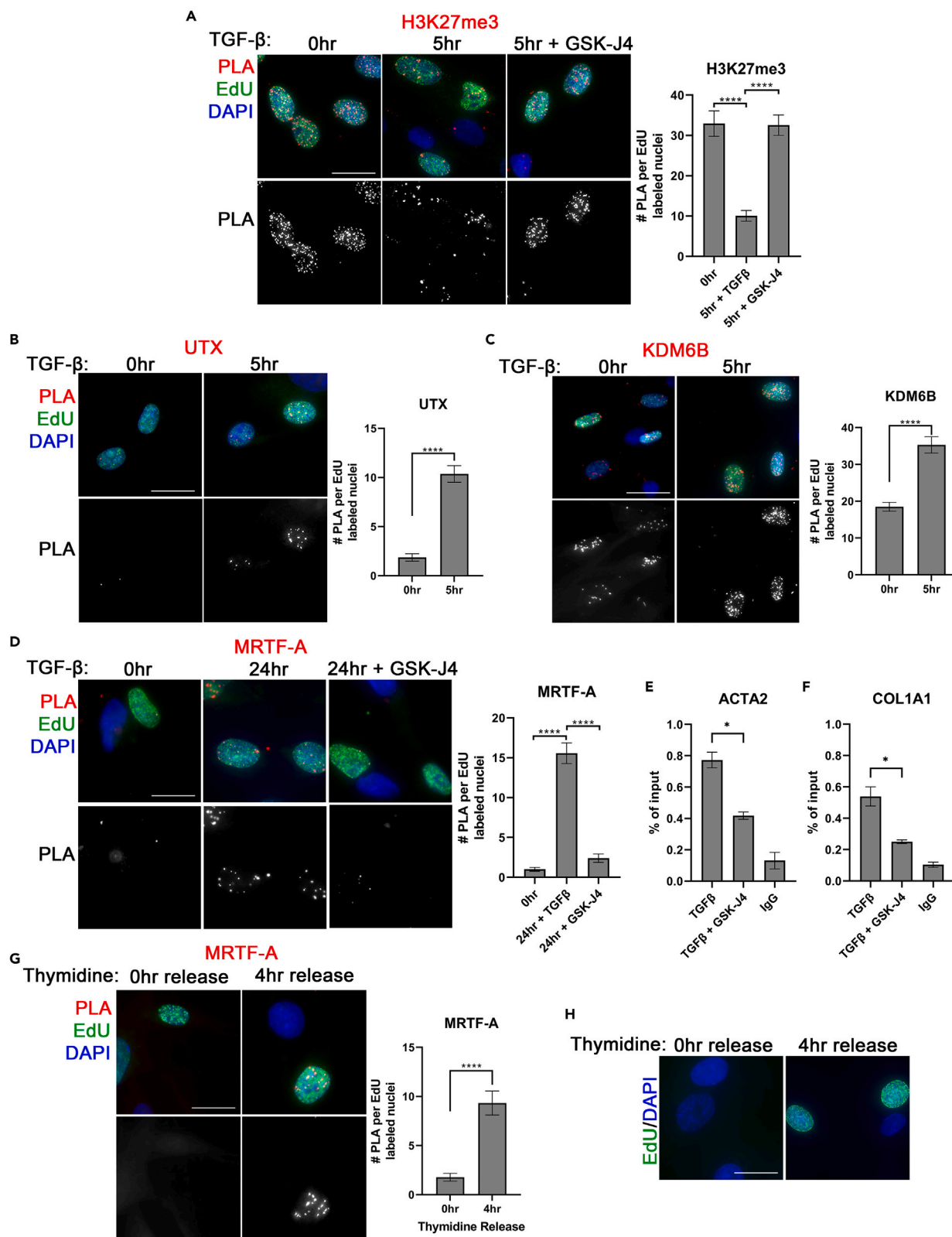


### Figure 6. The chromatin-based mechanism facilitated by UTX KDM activity is paralleled in primary lung fibroblasts

(A–D, G) Representative CAA images of primary HLF. Cells were labeled with EdU (green) for 20min and counterstained with DAPI (blue). PLA is shown in red and in split channel (black and white). Graphs depict the number of PLA per EdU labeled nuclei. Scale bar: 10  $\mu$ m. (A) Representative CAA images of H3K27me3 (red) at 0h and 5h post-treatment with 5 ng/mL TGF- $\beta$  in primary lung fibroblasts that were pretreated for 12h with GSK-J4 prior to the addition of TGF- $\beta$ . (B) Representative CAA images of UTX (red) at 0h and 5h post-stimulation with 5 ng/ml TGF- $\beta$  in primary HLF. (C) Representative CAA images for KDM6B (red) at 0h and 5h post-treatment with 5 ng/ml TGF $\beta$  in primary lung fibroblasts. (D) Representative CAA images of MRTF-A (red) at 0h and 24h post-stimulation with 5 ng/ml TGF- $\beta$  in primary HLF that were pretreated for 12h with GSK-J4 prior to addition of TGF- $\beta$ . (E and F) Chromatin was immunoprecipitated with MRTF-A antibody and IgG isotype control +/- GSK-J4. qPCR was performed for MRTF-A-containing genes: *ACTA2* and *COL1A1*. (G) Representative CAA images of MRTF-A (red) at 0h and 4h from thymidine release following 24h thymidine treatment in HLF. (H) Representative images of EdU (green) labeling at 0h and 4h after thymidine release following 24h thymidine treatment in HLF. Cultures were counterstained with DAPI (blue). Scale bar: 10  $\mu$ m. Representative data are expressed as average  $\pm$  SEM. \*\*\*\*p < 0.0001 \*p < 0.05 by one-way ANOVA with multiple comparisons (A, D) and unpaired t-test (B, C, E, F, G).

non-fibrotic wound repair, we treated *ex vivo* post-cataract surgery explants with GSK-J4 or vehicle immediately at the time of surgery until wounds in the center of the lens capsule heal, which typically occurs on day 3 post-injury.<sup>38–40</sup> We measured the wound area daily using methods previously described<sup>38,40</sup> and found that GSK-J4 treatment slowed but did not block normal wound healing (Figure S5B). To determine if cell proliferation is a contributing factor in slowed wound healing following GSK-J4 treatment, explants were also EdU-labeled on day 3. While a downward trend in EdU incorporation was observed with GSK-J4 treatment, cells in the center of capsule did not show a significant decrease in replication when treated with GSK-J4 (Figure S5C,  $p = 0.3820$ ). These findings along with the block of the fibrotic phenotype (Figures S5 and 5) suggests that UTX/KDM6B KDM activity has potential as a therapeutic target for preventing injury-induced fibrosis without a major impact on normal wound healing.

### The chromatin-based mechanism facilitated by UTX KDM activity is paralleled in primary lung fibroblasts

We next explored whether the chromatin-based mechanism driven by UTX/KDM6B KDM activity to decondense nascent chromatin structure to allow for pro-fibrotic TF binding in lens fibrosis is paralleled in lung fibrosis. For these studies, we used primary human lung fibroblasts (HLF) stimulated with TGF- $\beta$ 1 to induce transition to a myofibroblast. In uninduced primary HLF, we found that H3K27me3 recruitment to nascent DNA is quite robust, suggesting a highly condensed structure of nascent chromatin in proliferating lung fibroblasts (Figure 6A). However, when lung fibroblasts are induced with 5 ng/mL TGF- $\beta$ 1 for 5h to initiate transition to a myofibroblast fate, H3K27me3 association with nascent DNA is strongly decreased (Figure 6A,  $p < 0.0001$ ). These results suggest that the highly condensed structure of nascent chromatin in uninduced fibroblasts becomes significantly decondensed after 5h of TGF- $\beta$  induction toward a myofibroblast cell fate.

Similar to differentiating myofibroblast precursors in the lens fibrosis model (Figure 2C), we found that UTX is associated with nascent DNA at 5h post-treatment of primary HLF with TGF- $\beta$  (Figure 6B,  $p < 0.0001$ ), which occurs at the same time H3K27me3 recruitment to nascent DNA is decreased (Figure 6A). Interestingly, UTX is not associated with nascent DNA prior to treatment with TGF- $\beta$  (Figure 6B,  $p < 0.0001$ ), suggesting that TGF- $\beta$  treatment is needed to promote UTX binding to nascent DNA post-replication and to induce decondensed chromatin structure. We found that KDM6B is associated with nascent DNA prior to TGF- $\beta$  stimulation; however there is a large increase in recruitment of KDM6B following TGF- $\beta$  induction (Figure 6C,  $P = < 0.0001$ ). These data suggest that KDM6B KDM activity alone might not be sufficient to induce a decondensed structure of nascent chromatin but rather may have a cooperative role alongside UTX (Figure 6A). Matching our findings in the *ex vivo* post-cataract surgery lens model, we found that inhibiting UTX/KDM6B KDM activity with GSK-J4 led to a robust increase in H3K27me3 recruitment to nascent DNA (Figure 6A,  $p < 0.0001$ ). The results in both models imply that the UTX and/or KDM6B enzymatic activity is required to promote the decondensed state of post-replicative chromatin structure at early stages of reprogramming of the myofibroblast precursor cells.

Next, we determined whether MRTF-A binding to nascent DNA in HLF requires decondensed chromatin structure at the time of replication. In un-stimulated lung fibroblasts with condensed chromatin structure (Figure 6A), MRTF-A is not associated with nascent DNA (Figure 6D). Following treatment with TGF- $\beta$ , which leads to a decondensed structure of nascent chromatin, MRTF-A is abundantly recruited to the nascent DNA of lung

fibroblasts (Figure 6D,  $p < 0.0001$ ). Treatment with GSK-J4 to inhibit UTX/KDM6B KDM activity and condense nascent chromatin structure prevented the recruitment of MRTF-A to nascent DNA and to specific gene promoters of ACTA2 and COL1A1 in the HLF (Figure 6E,  $p < 0.0230$ ,  $F p = 0.0437$ ). In further support that MRTF-A is specifically recruited to nascent DNA during S phase, thymidine treated human primary lung fibroblasts blocked EdU incorporation (Figure 6H) and recruitment of MRTF-A (Figure 6G,  $p < 0.0001$ ). Upon thymidine release, replication resumed (Figure 6H) and MRTF-A rapidly accumulated to nascent DNA (Figure 6G,  $p < 0.0001$ ).

Taken together, our findings indicate that MRTF-A is recruited to decondensed nascent chromatin structure of myofibroblast precursors in both the lens and lung models exclusively during the early stages of DNA replication. Pharmacological inhibition of UTX/KDM6B KDM activity to condense H3K27me3-marked nascent chromatin blocks recruitment of MRTF-A to DNA.

### GSK-J4 prevents progression of pulmonary fibrosis in lung experimental models

We tested whether targeting UTX/KDM6B demethylase activity would also be effective in preventing lung fibrosis. To do so, we examined the effects of GSK-J4 treatment in two experimental models: the TGF- $\beta$ -stimulated primary HLF and the bleomycin-induced pulmonary fibrosis model, a clinically relevant mouse model for idiopathic pulmonary fibrosis (IPF) and other chronic fibrosis lung diseases.<sup>41</sup> First, we examined if GSK-J4 treatment could block pro-fibrotic gene expression following TGF- $\beta$  treatment to induce lung fibroblasts to differentiate into myofibroblasts. As expected, following 48h of TGF- $\beta$  treatment expression of pro-fibrotic genes was increased, including  $\alpha$ SMA (acta2) (Figure 7A,  $p < 0.0001$ ), COL1A1 (Figure 7B,  $p < 0.0001$ ), collagen type III alpha 1 chain (COL3A1) (Figure 7C,  $p < 0.0001$ ), and collagen type IV alpha 1 chain (COL4A1) (Figure 7D,  $p < 0.0001$ ) compared to untreated controls (Figures 7A–7D). However, compared to vehicle controls, GSK-J4 treatment of primary lung fibroblasts effectively suppressed TGF- $\beta$ -induced fibrotic gene expression of all tested fibrotic genes (Figures 7A–7D).

To validate these findings *in vivo*, mice were administered bleomycin into the lungs and 7 days later, subdermal osmotic pumps, containing either GSK-J4 or vehicle control, were implanted (Figure 7E, model & Table S1). Lung tissue was harvested 14 days post-implantation of pumps, i.e., 21 days post-bleomycin treatment, to investigate expression of pro-fibrotic genes by RNA analyses, to detect collagen fibers and lung morphology using Masson's trichrome, to assess quantitative changes in collagen content by measuring hydroxyproline (Figure 7E, model & Table S1). GSK-J4 treatment prevented bleomycin-induced upregulation of fibrotic genes including TGF- $\beta$ 1 (TGFB1) (Figure 7F,  $p < 0.0001$ ),  $\alpha$ SMA (ACTA2) (Figure 7G,  $p < 0.0001$ ), COL3A1 (Figure 7H,  $p < 0.0001$ ), and FN-EDA (FN1) (Figure 7I,  $p < 0.0001$ ). In the absence of bleomycin, lungs of vehicle-treated mice stained with Masson's trichrome showed no structural abnormalities or signs of fibrosis and exhibited the typical "lacy" lung structure (Figure 7J). In contrast, the lungs of mice treated with bleomycin alone (no GSK-J4) had large abnormal areas with dense cellular infiltration and intense areas of collagen accumulation, a heterogenic response, which is typical of this model<sup>42</sup> (Figures 7J and S6). Most importantly, mice that received bleomycin and were then treated with GSK-J4 showed little or no abnormal lung structure and no apparent fibrotic collagen deposition (Figure 7J); resembling the lungs of normal mice. Collagen content was further assessed by measuring hydroxyproline, a key feature of collagen that is critical for stabilizing the collagen triple helix. Animals exposed to bleomycin alone showed a trend toward an increase in hydroxyproline content (Figure 7K). The addition of GSK-J4 reduced the amount of hydroxyproline in the lung, which was similar to the control levels (Figure 7K), indicating a trend toward a decrease in collagen I content. Additionally, we determined the impact of GSK-J4 treatment on the pro-inflammatory response linked to promoting fibrosis.<sup>43</sup> Major differences in T cell numbers were not detected between bleomycin and GSKJ4 treatment even though there was a paucity of cells (data not shown). While immunofluorescence revealed no major changes in macrophage infiltration (Figures S7A and S7B), it was found by RT-qPCR that the pro-inflammatory response was decreased by GSK-J4 (Figures S7B–S7E,  $p < 0.0001$ ). Furthermore, genes related to suppressing an inflammatory response were upregulated following GSK-J4 treatment (Figures S7F and S7G,  $p < 0.0001$ ). Altogether, these findings show that treatment with GSK-J4 effectively prevented the development of lung fibrosis in mice.

## DISCUSSION

Despite our knowledge of the key features governing the initiation of fibrosis, the core molecular events driving reprogramming of precursor cells to disease-causing myofibroblasts are less understood. In this study, we identified a nascent chromatin-based mechanism driven by UTX/KDM6B KDM activity that

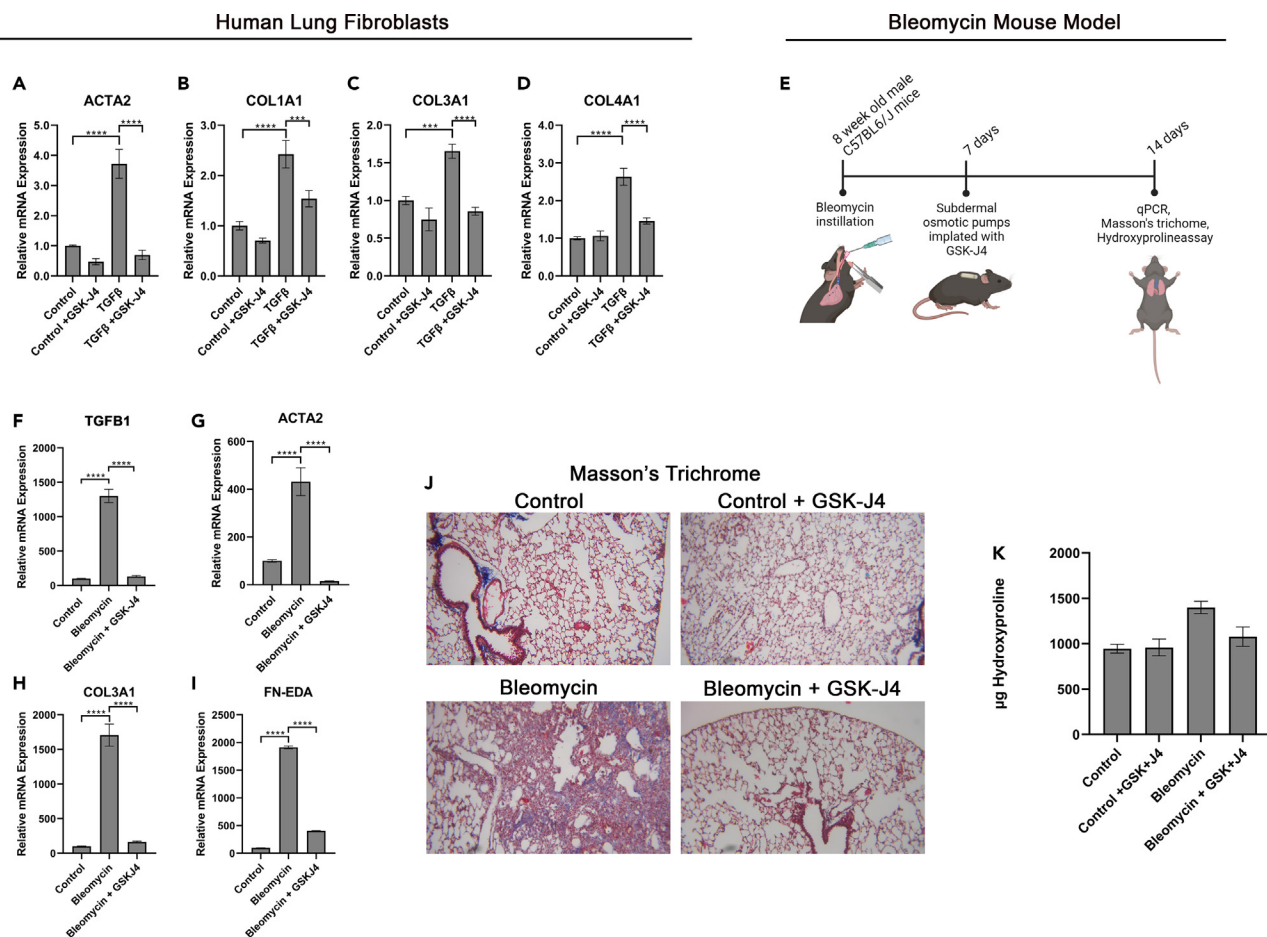


**Figure 7. GSK-J4 prevents progression of pulmonary fibrosis in lung experimental models**

(A–D) Relative gene expression (normalized to *GAPDH*) of pro-fibrotic genes for HLF either untreated, treated with GSK-J4 for 12h, induced with 5 ng/ml of TGF- $\beta$  for 48h, or treated with both GSK-J4 and TGF- $\beta$ .

(E) Schematic diagram of timeline depicting treatment and analyses for *in vivo* bleomycin mouse model studies.

(F–I) Relative mRNA expression of pro-fibrotic genes (normalized to  $\beta$ -Actin) from mice with bleomycin-induced pulmonary fibrosis and control treated with or without GSK-J4.

(J) Representative images of Masson's trichrome stained lungs divided into 4 treatment groups: saline control, GSK-J4 control, bleomycin-treated mice, and GSK-J4 and bleomycin treated mice.

(K) Hydroxyproline content obtained from left lobes of mice from 4 treatment groups: saline control, GSK-J4 control, bleomycin-treated mice, and GSK-J4 and bleomycin treated mice. Representative data are presented as average  $\pm$  SEM from 2 independent experiments (A–D). \*\*\*\* $p < 0.0001$  by one-way ANOVA with multiple comparisons. Data is expressed as average  $\pm$  SEM from using multiple mice for each condition performed in triplicate (F–I).

\*\*\*\* $p < 0.0001$  by one-way ANOVA with multiple comparisons. Data is expressed as average  $\pm$  SEM from using multiple mice for each condition performed in triplicate (see table for  $n$ ).

underlies reprogramming of CD44<sup>+</sup> progenitor cells and lung fibroblasts to myofibroblasts. Additionally, we determined whether manipulation of this mechanism by pharmacologically targeting UTX/KDM6B KDM activity would prevent myofibroblast emergence and the fibrotic phenotype. Our results show that UTX/KDM6B KDM activity is fundamental to driving the fibrotic process and demonstrate that UTX/KDM6B KDM activity is an attractive target for the prevention of organ fibrosis.

While lineage-specific TFs must bind to repressed genes to activate new transcriptional programs, it is not clear mechanistically how it occurs, since most TFs, including pioneer factors, cannot bind to condensed regions of chromatin, which are marked by H3K27me3.<sup>25</sup> Our work in myofibroblast precursor cells shows that at early stages following induction of fibrosis, condensed, H3K27me3-marked chromatin undergoes decondensation during DNA replication. This mechanism is driven by the activity of the H3K27me3 KDM enzymes UTX/KDM6B, which remove this histone mark, thus leading to transient decondensation of nascent

chromatin, and creating an opportunity for the pro-fibrotic TF MRTFA to bind and activate repressed genes. This discovery is in line with our previous findings that UTX KDM activity is necessary to induce decondensed nascent chromatin structure to allow for differentiation of hematopoietic and embryonic stem cells.<sup>23,24</sup> Similarly, it was previously shown that embryonic stem cell differentiation into endoderm lineages is facilitated by UTX and KDM6B.<sup>44</sup> It was more recently reported that H3K27me3 demethylation by UTX is required for germinal center B cell differentiation.<sup>45</sup> Our work here, in support with the previous studies, illustrates a period of decondensed nascent chromatin structure created by UTX/KDM6B that facilitates TF binding to drive precursor cell reprogramming to myofibroblasts responsible for fibrotic disease.

TGF- $\beta$  is classically considered a master regulator of myofibroblast differentiation and fibrosis.<sup>46</sup> Previously, using the *ex vivo* post-cataract surgery model, we demonstrated that CD44<sup>+</sup> leader cell transition to an  $\alpha$ SMA-expressing myofibroblast is under the control of endogenous TGF- $\beta$ .<sup>30</sup> Similarly, the primary HLF used in this study here require TGF- $\beta$  treatment to undergo transition to a myofibroblast which is a common aspect of many *in vitro* fibrosis models. Our findings in CD44<sup>+</sup> progenitor cells and primary HLF reveal that during the TGF- $\beta$ -induced transition to a myofibroblast cell type, UTX/KDM6B facilitates decondensation of the post-replicative chromatin structure. TGF- $\beta$ 1 treatment in HLF induces recruitment of UTX and increased KDM6B recruitment to nascent DNA coincident with a decrease in H3K27me3 accumulation on nascent DNA. In support of our work here, a study of diabetic-induced fibrosis in renal mesangial cells found that TGF- $\beta$  treatment upregulated UTX and KDM6B mRNA levels via RT-qPCR and suppressed H3K27me3 levels on pro-inflammatory genes by ChIP.<sup>47</sup> This study provides support for our work here revealing that TGF- $\beta$ -induced transition to a myofibroblast increases UTX and KDM6B recruitment to nascent DNA to decondense chromatin structure making it amenable for the adoption of a new pro-fibrotic transcription program.

Our RNA-seq analysis using the *ex vivo* post-cataract surgery lens explants treated with GSK-J4 establishes UTX/KDM6B KDM activity as fundamental to acquisition of the pro-fibrotic transcriptome. We propose that condensing chromatin structure with GSK-J4 prevents pro-fibrotic TF binding, such as MRTF-A, to downregulate gene sets associated with creating and driving the fibrotic phenotype. While it was outlined above that TGF- $\beta$  has the potential to influence UTX/KDM6B expression/recruitment, we discovered that inhibition of UTX/KDM6B KDM activity results in downregulation of TGF- $\beta$ 1, TGF- $\beta$  receptor II and genes associated with mechanisms that activate latent TGF- $\beta$ .<sup>13,48</sup> Furthermore, treatment with GSK-J4 led to a downregulation of TGF $\beta$  mRNA levels in the bleomycin lung model. These data identify a noteworthy ability for UTX/KDM6B KDM activity to control TGF- $\beta$  activation and signaling. Similarly, in an aging study using hematopoietic stem-progenitor cells, UTX deficient mice resulted in a significant downregulation of the TGF- $\beta$  signaling pathway gene set.<sup>49</sup> Moreover, knockdown of KDM6B in lung carcinoma epithelial cells impaired TGF $\beta$  induced phosphorylation of downstream TFs, Mothers against decapentaplegic 2 and 3 (Smad2/Smad3).<sup>50</sup> Contrary to our work and the study above, it was found that UTX knockout in human embryonic stem cell-derived neurons led to increased enrichment of the TGF- $\beta$  signaling pathway gene set.<sup>51</sup> We speculate that while UTX/KDM6B appears critical for regulating TGF- $\beta$  activation and signaling in our models, there might be key differences in their regulation in some tissues.

In addition to the downregulation of TGF- $\beta$  activation and signaling, we also found that GSK-J4 treatment downregulated genes that would impact stiffness-dependent mechanisms critical to driving fibrosis. GSK-J4 directly impacted changes in rigidity of the microenvironment by blocking genes involved in the *de novo* expression, fibrillogenesis, and cross-linking of matrices. Importantly, we found that GSK-J4 leads to downregulation of expression of COL1A1 and COL1A2, while also downregulating genes necessary for collagen synthesis like PLOD2<sup>52</sup> and structural organization such as LOXL1, which is key to the crosslinking of collagen fibers.<sup>53</sup> Furthermore, GSK-J4 treatment downregulated genes involved in integrin mediated stiffness-dependent signals from the ECM microenvironment to the cytoskeleton of the cell. These include downregulation of specific fibronectin and collagen I binding integrin receptors and regulators of the mechanosensitive focal adhesion protein complexes through which integrins signal. Additionally, genes that compose constituents of the actin cytoskeleton and regulators of actin cytoskeletal organization, including assembly of the actomyosin stress fiber-mediated contractile machinery were downregulated. These findings show that UTX/KDM6B regulate activation of genes that are essential to the exchange of information between the stiff microenvironment and mechanosensing machinery of the cell to drive fibrotic disease. Together these studies reveal UTX/KDM6B master regulators of the fibrotic phenotype and strongly support the UTX/KDM6B KDM activity as an attractive all-encompassing therapeutic target to block acquisition of the fibrotic transcriptome.

Our studies reveal an interesting relationship between UTX/KDM6B KDM activity and DNA replication. We found that a chromatin decondensation-based mechanism controlled by UTX/KDM6B occurs at the time of DNA replication to drive the fibrotic process in both lens and lung fibrosis models. Importantly, we show that recruitment of TFs, specifically MRTF-A, only happens to decondensed chromatin structure just after DNA replication in the S-phase. Accordingly, inhibiting UTX/KDM6B KDM activity condenses chromatin structure and prevents binding of MRTF-A on nascent DNA. These key experiments reveal that UTX/KDM6B KDM inhibition quickly results in condensed chromatin structure and blocks TF binding in replicating precursor cells. While our experiments reveal that DNA-replication is necessary for allowing this UTX/KDM6B-facilitated chromatin-based mechanism to occur, our RNA-seq analysis in the *ex vivo* post-cataract surgery lens model also reveals an ability for UTX/KDM6B to regulate DNA-replication. UTX/KDM6B KDM inhibition resulted in a downregulation of ORC and MCM genes that are essential for DNA replication<sup>34</sup> and prevented leader cells associated with the fibrotic phenotype from proliferating on day 3 post-injury. These findings are in line with previous studies showing that UTX and/or KDM6B has an important role in regulating proliferation but whether it promotes or blocks proliferation depends on the cellular context.<sup>54–58</sup> Our findings here expand our understanding of how UTX/KDM6B KDM activity can regulate gene expression through both blocking TF binding by condensing chromatin structure on replicating DNA while preventing new opportunities for TF binding by interrupting DNA replication.

In summary, our work reveals that differentiation of myofibroblast precursor cells is dependent on a decondensed structure of post-replicative chromatin induced by UTX/KDM6B KDM activity to allow for pro-fibrotic TF binding to initiate the fibrotic phenotype. There are some interesting observations in our studies that open up new areas of potential investigation. One finding is the relationship between UTX/KDM6B and TGF- $\beta$  that shows an ability for TGF- $\beta$  to induce H3K27 KDM enzyme recruitment and conversely that H3K27 KDM enzymes regulate genes of the TGF- $\beta$  pathway. Future studies are needed to fully understand the relationship between KDM enzymes and TGF- $\beta$ 1 and how they operate in fibrosis including whether the anti-fibrotic impact of GSK-J4 could be due in part to its effects on blocking TGF- $\beta$  signaling as well as effects on primary fibrotic gene targets of UTX/KDM6B. Overall, our findings in two distinct fibrotic tissue types provide a new molecular understanding for how fibrosis is initiated and features a new potential therapeutic target, UTX/KDM6B, for prevention of organ fibrosis.

### Limitations of the study

While our findings identify a new chromatin-based mechanism that underlies the initiation of fibrosis, there are a few limitations of our study. We pinpoint a major role for UTX/KDM6B to demethylate H3K27me3 and decondense chromatin structure to allow for MRTF-A recruitment to nascent DNA to drive pro-fibrotic gene expression. However, we do not know what other TFs are recruited to decondensed nascent chromatin to activate other genes involved in fibrosis. Our studies use CAA to investigate association of proteins on short nascent DNA in all regions of the genome, which cannot be detected in bulk chromatin. These studies require very specific nascent chromatin-targeted assays, which cannot be accomplished by conventional techniques that assess bulk chromatin.

### STAR★METHODS

Detailed methods are provided in the online version of this paper and include the following:

- KEY RESOURCES TABLE
- RESOURCE AVAILABILITY
  - Lead contact
  - Materials availability
  - Data and code availability
- EXPERIMENTAL MODEL AND STUDY PARTICIPANT DETAILS
  - *Ex vivo* post cataract surgery cultures
  - Pediatric human lens explants
  - Primary human lung fibroblasts
  - Bleomycin mouse model
- METHOD DETAILS
  - Immunofluorescence staining and confocal imaging
  - Hydroxyproline
  - Masson's trichrome

- Western blot analysis
- Chromatin assembly assay and analysis
- Treatment with thymidine
- Proliferation
- Inhibition of H3K27 KDMs by GSK-J4
- RNA-seq analysis
- Chromatin immunoprecipitation
- Wound healing
- Gene expression analysis by RT-qPCR
- **QUANTIFICATION AND STATISTICAL ANALYSIS**

## SUPPLEMENTAL INFORMATION

Supplemental information can be found online at <https://doi.org/10.1016/j.isci.2023.106570>.

## ACKNOWLEDGMENTS

The authors would like to thank Heather M. Paulson for her technical assistance. This work was supported by National Institutes of Health EY026159 to JLW and AM, 5R01AI125650 and GM075141 to AM and Falk grant 080-13007-U27401 to RS and AM. MB was supported by the National Institute of Arthritis and Musculoskeletal and Skin Disease of the National Institute of Health T32 AR 52273-15. The Foerderer Fund (AVL), The Robison D. Harley, MD Endowed Chair in Pediatric Ophthalmology and Ocular Genetics (AVL), the Adeline Lutz - Steven S.T. Ching, M.D. Distinguished Professorship in Ophthalmology (AVL) and an unrestricted grant from Research to Prevent Blindness to the Department of Ophthalmology at the University of Rochester (AVL).

## AUTHOR CONTRIBUTIONS

Conceptualization: M.D.B., S.P., R.S., J.R., A.M., and J.L.W.. Methodology: J.L.W., A.M., M.D.B., R.S., S.P., and A.V.L.. Investigation: M.D.B., S.P., P.J.W., and E.M.. Supervision: J.L.W., A.M., R.S., and J.R.. Writing-Original Draft: M.D.B., and J.L.W.. Writing- Review & Editing: M.D.B., A.M., A.V.L., E.M., S.P., J.R., R.S., J.L.W., and P.W.

## DECLARATION OF INTERESTS

J.L.W., A.M., and S.P. are coinventors on patent application 16/335,716 entitled "Drug-induced epigenetic remodeling to prevent fibrosis".

Received: September 27, 2022

Revised: March 3, 2023

Accepted: March 29, 2023

Published: April 6, 2023

## REFERENCES

1. Henderson, N.C., Rieder, F., and Wynn, T.A. (2020). Fibrosis: from mechanisms to medicines. *Nature* 587, 555–566. <https://doi.org/10.1038/s41586-020-2938-9>.
2. Wynn, T.A., and Ramalingam, T.R. (2012). Mechanisms of fibrosis: therapeutic translation for fibrotic disease. *Nat. Med.* 18, 1028–1040. <https://doi.org/10.1038/nm.2807>.
3. Rockey, D.C., Bell, P.D., and Hill, J.A. (2015). Fibrosis—A common pathway to organ injury and failure. *N. Engl. J. Med.* 373, 96. <https://doi.org/10.1056/NEJMc1504848>.
4. Hinz, B. (2016). Myofibroblasts. *Exp. Eye Res.* 142, 56–70. <https://doi.org/10.1016/j.exer.2015.07.009>.
5. Wynn, T.A. (2008). Cellular and molecular mechanisms of fibrosis. *J. Pathol.* 214, 199–210. <https://doi.org/10.1002/path.2277>.
6. Hinz, B., and Lagares, D. (2020). Evasion of apoptosis by myofibroblasts: a hallmark of fibrotic diseases. *Nat. Rev. Rheumatol.* 16, 11–31. <https://doi.org/10.1038/s41584-019-0324-5>.
7. Hinz, B., Phan, S.H., Thannickal, V.J., Galli, A., Bochaton-Piallat, M.L., and Gabbiani, G. (2007). The myofibroblast: one function, multiple origins. *Am. J. Pathol.* 170, 1807–1816. <https://doi.org/10.2353/ajpath.2007.070112>.
8. Micallef, L., Vedrenne, N., Billet, F., Coulomb, B., Darby, I.A., and Desmoulière, A. (2012). The myofibroblast, multiple origins for major roles in normal and pathological tissue repair. *Fibrogenesis Tissue Repair* 5, S5. <https://doi.org/10.1186/1755-1536-5-S1-S5>.
9. Small, E.M., Thatcher, J.E., Sutherland, L.B., Kinoshita, H., Gerard, R.D., Richardson, J.A., Dimaio, J.M., Sadek, H., Kuwahara, K., and Olson, E.N. (2010). Myocardin-related transcription factor-a controls myofibroblast activation and fibrosis in response to myocardial infarction. *Circ. Res.* 107, 294–304. <https://doi.org/10.1161/CIRCRESAHA.110.223172>.
10. Werner, S., Lützkendorf, J., Müller, T., Müller, L.P., and Posern, G. (2019). MRTF-A controls myofibroblastic differentiation of human multipotent stromal cells and their tumour-supporting function in xenograft models. *Sci.*

- Rep. 9, 11725. <https://doi.org/10.1038/441598-019-48142-z>.
11. Akhurst, R.J., and Hata, A. (2012). Targeting the TGF $\beta$  signalling pathway in disease. *Nat. Rev. Drug Discov.* 11, 790–811. <https://doi.org/10.1038/nrd3810>.
12. Crider, B.J., Risinger, G.M., Jr., Haaksma, C.J., Howard, E.W., and Tomasek, J.J. (2011). Myocardin-related transcription factors A and B are key regulators of TGF- $\beta$ 1-induced fibroblast to myofibroblast differentiation. *J. Invest. Dermatol.* 131, 2378–2385. <https://doi.org/10.1038/jid.2011.219>.
13. Hinz, B. (2009). Tissue stiffness, latent TGF- $\beta$ 1 activation, and mechanical signal transduction: implications for the pathogenesis and treatment of fibrosis. *Curr. Rheumatol. Rep.* 11, 120–126. <https://doi.org/10.1007/s11926-009-0017-1>.
14. Tschumperlin, D.J., Ligresti, G., Hilscher, M.B., and Shah, V.H. (2018). Mechanosensing and fibrosis. *J. Clin. Invest.* 128, 74–84. <https://doi.org/10.1172/JCI93561>.
15. Velasquez, L.S., Sutherland, L.B., Liu, Z., Grinnell, F., Kamm, K.E., Schneider, J.W., Olson, E.N., and Small, E.M. (2013). Activation of MRTF-A-dependent gene expression with a small molecule promotes myofibroblast differentiation and wound healing. *Proc. Natl. Acad. Sci. USA* 110, 16850–16855. <https://doi.org/10.1073/pnas.1316741110>.
16. Bell, O., Schwaiger, M., Oakeley, E.J., Lienert, F., Beisel, C., Stadler, M.B., and Schübeler, D. (2010). Accessibility of the *Drosophila* genome discriminates PcG repression, H4K16 acetylation and replication timing. *Nat. Struct. Mol. Biol.* 17, 894–900. <https://doi.org/10.1038/nsmb.1825>.
17. Shlyueva, D., Stampfel, G., and Stark, A. (2014). Transcriptional enhancers: from properties to genome-wide predictions. *Nat. Rev. Genet.* 15, 272–286. <https://doi.org/10.1038/nrg3682>.
18. Yuan, W., Wu, T., Fu, H., Dai, C., Wu, H., Liu, N., Li, X., Xu, M., Zhang, Z., Niu, T., et al. (2012). Dense chromatin activates Polycomb repressive complex 2 to regulate H3 lysine 27 methylation. *Science* 337, 971–975. <https://doi.org/10.1126/science.1225237>.
19. Barski, A., Cuddapah, S., Cui, K., Roh, T.Y., Schones, D.E., Wang, Z., Wei, G., Chepelev, I., and Zhao, K. (2007). High-resolution profiling of histone methylations in the human genome. *Cell* 129, 823–837. <https://doi.org/10.1016/j.cell.2007.05.009>.
20. Alabert, C., and Groth, A. (2012). Chromatin replication and epigenome maintenance. *Nat. Rev. Mol. Cell Biol.* 13, 153–167. <https://doi.org/10.1038/nrm3288>.
21. López-Jiménez, E., and González-Aguilera, C. (2022). Role of chromatin replication in transcriptional plasticity, cell differentiation and disease. *Genes* 13, 1002. <https://doi.org/10.3390/genes13061002>.
22. McKnight, S.L., and Miller, O.L., Jr. (1977). Electron microscopic analysis of chromatin replication in the cellular blastoderm *Drosophila melanogaster* embryo. *Cell* 12, 795–804. [https://doi.org/10.1016/0092-8674\(77\)90278-1](https://doi.org/10.1016/0092-8674(77)90278-1).
23. Petruk, S., Cai, J., Sussman, R., Sun, G., Kovermann, S.K., Mariani, S.A., Calabretta, B., McMahon, S.B., Brock, H.W., Iacovitti, L., and Mazo, A. (2017). Delayed accumulation of H3K27me3 on nascent DNA is essential for recruitment of transcription factors at early stages of stem cell differentiation. *Mol. Cell* 66, 247–257.e5. <https://doi.org/10.1016/j.molcel.2017.03.006>.
24. Petruk, S., Mariani, S.A., De Dominicis, M., Porazzi, P., Minieri, V., Cai, J., Iacovitti, L., Flomenberg, N., Calabretta, B., and Mazo, A. (2017). Structure of nascent chromatin is essential for hematopoietic lineage specification. *Cell Rep.* 19, 295–306. <https://doi.org/10.1016/j.celrep.2017.03.035>.
25. Iwafuchi-Doi, M., and Zaret, K.S. (2016). Cell fate control by pioneer transcription factors. *Development* 143, 1833–1837. <https://doi.org/10.1242/dev.133900>.
26. Walker, J.L., Zhai, N., Zhang, L., Bleaken, B.M., Wolff, I., Gerhart, J., George-Weinstein, M., and Menko, A.S. (2010). Unique precursors for the mesenchymal cells involved in injury response and fibrosis. *Proc. Natl. Acad. Sci. USA* 107, 13730–13735. <https://doi.org/10.1073/pnas.0910382107>.
27. Walker, J.L., Wolff, I.M., Zhang, L., and Menko, A.S. (2007). Activation of SRC kinases signals induction of posterior capsule opacification. *Invest. Ophthalmol. Vis. Sci.* 48, 2214–2223. <https://doi.org/10.1167/iov.06-1059>.
28. Menko, A.S., DeDreu, J., Logan, C.M., Paulson, H., Levin, A.V., and Walker, J.L. (2021). Resident immune cells of the avascular lens: mediators of the injury and fibrotic response of the lens. *Faseb. J.* 35, e21341. <https://doi.org/10.1096/fj.202002200R>.
29. Walker, J.L., Bleaken, B.M., Romisher, A.R., Alnwibit, A.A., and Menko, A.S. (2018). In wound repair vimentin mediates the transition of mesenchymal leader cells to a myofibroblast phenotype. *Mol. Biol. Cell* 29, 1555–1570. <https://doi.org/10.1091/mbc.E17-06-0364>.
30. Basta, M.D., Paulson, H., and Walker, J.L. (2021). The local wound environment is a key determinant of the outcome of TGF $\beta$  signaling on the fibrotic response of CD44(+) leader cells in an ex vivo post-cataract-surgery model. *Exp. Eye Res.* 213, 108829. <https://doi.org/10.1016/j.exer.2021.108829>.
31. Dalton, S. (2015). Linking the cell cycle to cell fate decisions. *Trends Cell Biol.* 25, 592–600. <https://doi.org/10.1016/j.tcb.2015.07.007>.
32. Petruk, S., Sedkov, Y., Johnston, D.M., Hodgson, J.W., Black, K.L., Kovermann, S.K., Beck, S., Canaani, E., Brock, H.W., and Mazo, A. (2012). TrxG and PcG proteins but not methylated histones remain associated with DNA through replication. *Cell* 150, 922–933. <https://doi.org/10.1016/j.cell.2012.06.046>.
33. Kruidenier, L., Chung, C.W., Cheng, Z., Liddle, J., Che, K., Joberty, G., Bantscheff, M., Bountra, C., Bridges, A., Diallo, H., et al. (2012). A selective jumonji H3K27 demethylase inhibitor modulates the proinflammatory macrophage response. *Nature* 488, 404–408. <https://doi.org/10.1038/nature11262>.
34. Stillman, B. (1996). Cell cycle control of DNA replication. *Science* 274, 1659–1664. <https://doi.org/10.1126/science.274.5293.1659>.
35. Apple, D.J., Solomon, K.D., Tetz, M.R., Assia, E.I., Holland, E.Y., Legler, U.F., Tsai, J.C., Castaneda, V.E., Hoggatt, J.P., and Kostick, A.M. (1992). Posterior capsule opacification. *Surv. Ophthalmol.* 37, 73–116. [https://doi.org/10.1016/0039-6257\(92\)90073-3](https://doi.org/10.1016/0039-6257(92)90073-3).
36. Awasthi, N., Guo, S., and Wagner, B.J. (2009). Posterior capsular opacification: a problem reduced but not yet eradicated. *Arch. Ophthalmol.* 127, 555–562. <https://doi.org/10.1001/archophthalmol.2009.3>.
37. Spierer, A., Desatnik, H., and Blumenthal, M. (1999). Refractive status in children after long-term follow up of cataract surgery with intraocular lens implantation. *J. Pediatr. Ophthalmol. Strabismus* 36, 25–29. <https://doi.org/10.3928/0191-3913-19990101-06>.
38. Walker, J.L., Bleaken, B.M., Wolff, I.M., and Menko, A.S. (2015). Establishment of a clinically relevant ex vivo mock cataract surgery model for investigating epithelial wound repair in a native microenvironment. *J. Vis. Exp.* 100, e52886. <https://doi.org/10.3791/52886>.
39. Bleaken, B.M., Menko, A.S., and Walker, J.L. (2016). Cells activated for wound repair have the potential to direct collective invasion of an epithelium. *Mol. Biol. Cell* 27, 451–465. <https://doi.org/10.1091/mbc.E15-09-0615>.
40. Menko, A.S., Bleaken, B.M., Libowitz, A.A., Zhang, L., Stepp, M.A., and Walker, J.L. (2014). A central role for vimentin in regulating repair function during healing of the lens epithelium. *Mol. Biol. Cell* 25, 776–790. <https://doi.org/10.1091/mbc.E12-12-0900>.
41. Tashiro, J., Rubio, G.A., Limper, A.H., Williams, K., Elliot, S.J., Ninou, I., Aidinis, V., Tzouvelekis, A., and Glassberg, M.K. (2017). Exploring animal models that resemble idiopathic pulmonary fibrosis. *Front. Med.* 4, 118. <https://doi.org/10.3389/fmed.2017.00118>.
42. Chua, F., Gauldie, J., and Laurent, G.J. (2005). Pulmonary fibrosis: searching for model answers. *Am. J. Respir. Cell Mol. Biol.* 33, 9–13. <https://doi.org/10.1165/rcmb.2005-0062TR>.
43. Mack, M. (2018). Inflammation and fibrosis. *Matrix Biol.* 68–69, 106–121. <https://doi.org/10.1016/j.matbio.2017.11.010>.
44. Jiang, W., Wang, J., and Zhang, Y. (2013). Histone H3K27me3 demethylases KDM6A and KDM6B modulate definitive endoderm differentiation from human ESCs by regulating WNT signaling pathway. *Cell Res.* 23, 122–130. <https://doi.org/10.1038/cr.2012.119>.

45. Haniuda, K., Fukao, S., and Kitamura, D. (2020). Metabolic reprogramming induces germinal center B cell differentiation through Bcl6 locus remodeling. *Cell Rep.* 33, 108333. <https://doi.org/10.1016/j.celrep.2020.108333>.
46. Lodyga, M., and Hinz, B. (2020). TGF-beta1 - a truly transforming growth factor in fibrosis and immunity. *Semin. Cell Dev. Biol.* 101, 123–139. <https://doi.org/10.1016/j.semcdb.2019.12.010>.
47. Jia, Y., Reddy, M.A., Das, S., Oh, H.J., Abdollahi, M., Yuan, H., Zhang, E., Lanting, L., Wang, M., and Natarajan, R. (2019). Dysregulation of histone H3 lysine 27 trimethylation in transforming growth factor-beta1-induced gene expression in mesangial cells and diabetic kidney. *J. Biol. Chem.* 294, 12695–12707. <https://doi.org/10.1074/jbc.RA119.007575>.
48. Robertson, I.B., Horiguchi, M., Zilberberg, L., Dabovic, B., Hadjiolova, K., and Rifkin, D.B. (2015). Latent TGF-beta-binding proteins. *Matrix Biol.* 47, 44–53. <https://doi.org/10.1016/j.matbio.2015.05.005>.
49. Sera, Y., Nakata, Y., Ueda, T., Yamasaki, N., Koide, S., Kobayashi, H., Ikeda, K.I., Kobatake, K., Iwasaki, M., Oda, H., et al. (2021). UTX maintains the functional integrity of the murine hematopoietic system by globally regulating aging-associated genes. *Blood* 137, 908–922. <https://doi.org/10.1182/blood.2019001044>.
50. Lee, S.H., Kim, O., Kim, H.J., Hwangbo, C., and Lee, J.H. (2021). Epigenetic regulation of TGF-beta-induced EMT by JMJD3/KDM6B histone H3K27 demethylase. *Oncogenesis* 10, 17. <https://doi.org/10.1038/s41389-021-00307-0>.
51. Tang, Q.Y., Zhang, S.F., Dai, S.K., Liu, C., Wang, Y.Y., Du, H.Z., Teng, Z.Q., and Liu, C.M. (2020). UTX regulates human neural differentiation and dendritic morphology by resolving bivalent promoters. *Stem Cell Rep.* 15, 439–453. <https://doi.org/10.1016/j.stemcr.2020.06.015>.
52. van der Slot, A.J., Zuurmond, A.M., Bardoel, A.F.J., Wijmenga, C., Pruijs, H.E.H., Sillence, D.O., Brinckmann, J., Abraham, D.J., Black, C.M., Verzijl, N., et al. (2003). Identification of PLOD2 as telopeptide lysyl hydroxylase, an important enzyme in fibrosis. *J. Biol. Chem.* 278, 40967–40972. <https://doi.org/10.1074/jbc.M307380200>.
53. Tjin, G., White, E.S., Faiz, A., Sicard, D., Tschumperlin, D.J., Mahar, A., Kable, E.P.W., and Burgess, J.K. (2017). Lysyl oxidases regulate fibrillar collagen remodelling in idiopathic pulmonary fibrosis. *Dis. Model. Mech.* 10, 1301–1312. <https://doi.org/10.1242/dmm.030114>.
54. Kim, J.H., Sharma, A., Dhar, S.S., Lee, S.H., Gu, B., Chan, C.H., Lin, H.K., and Lee, M.G. (2014). UTX and MLL4 coordinately regulate transcriptional programs for cell proliferation and invasiveness in breast cancer cells. *Cancer Res.* 74, 1705–1717. <https://doi.org/10.1158/0008-5472.CAN-13-1896>.
55. Liu, J., Mercher, T., Scholl, C., Brumme, K., Gilliland, D.G., and Zhu, N. (2012). A functional role for the histone demethylase UTX in normal and malignant hematopoietic cells. *Exp. Hematol.* 40, 487–498.e3. <https://doi.org/10.1016/j.exphem.2012.01.017>.
56. Pediconi, N., Salerno, D., Lupacchini, L., Angrisani, A., Peruzzi, G., De Smaele, E., Levrero, M., and Belloni, L. (2019). EZH2, JMJD3, and UTX epigenetically regulate hepatic plasticity inducing retro-differentiation and proliferation of liver cells. *Cell Death Dis.* 10, 518. <https://doi.org/10.1038/s41419-019-1755-2>.
57. Romani, M., Daga, A., Forlani, A., Pistillo, M.P., and Banelli, B. (2019). Targeting of histone demethylases KDM5A and KDM6B inhibits the proliferation of temozolomide-resistant glioblastoma cells. *Cancers* 11, 878. <https://doi.org/10.3390/cancers11060878>.
58. Qin, M., Han, F., Wu, J., Gao, F.X., Li, Y., Yan, D.X., He, X.M., Long, Y., Tang, X.P., Ren, D.L., et al. (2021). KDM6B promotes ESCC cell proliferation and metastasis by facilitating C/EBPbeta transcription. *BMC Cancer* 21, 559. <https://doi.org/10.1186/s12885-021-08282-w>.
59. Romero, F., Hong, X., Shah, D., Kallen, C.B., Rosas, I., Guo, Z., Schriener, D., Barta, J., Shaghghi, H., Hoek, J.B., et al. (2018). Lipid synthesis is required to resolve endoplasmic reticulum stress and limit fibrotic responses in the lung. *Am. J. Respir. Cell Mol. Biol.* 59, 225–236. <https://doi.org/10.1165/rcmb.2017-0340OC>.

## STAR★METHODS

### KEY RESOURCES TABLE

REAGENT or RESOURCE	SOURCE	IDENTIFIER
<b>Antibodies</b>		
Anti-Actin, alpha-smooth muscle (1A4) antibody	Sigma Aldrich	Cat# A2547, RRID:AB_476701
Anti-Actin, alpha-smooth muscle antibody	Abcam	Cat# ab5694, RRID:AB_2223021
Anti-MK11/MRTF-A antibody	Abcam	Cat# ab49311, RRID:AB_2235171
Anti- MRTF-A (H-140) antibody	Santa Cruz Biotechnology	Cat# sc-32909, RRID:AB_2142495
Anti-Fibronectin ED-A domain (1ST-9) antibody	Santa Cruz Biotechnology	Cat# sc-59826, RRID:AB_783389
Anti-Collagen, Type I pro-peptide (SP1.D8) antibody	Developmental Studies Hybridoma Bank - Furthmayr, H.	Cat# SP1.D8, RRID:AB_528438
Anti-UTX (D3Q11) antibody	Cell Signaling Technology	Cat# 33510, RRID:AB_2721244
Anti-KDM6B antibody	Thermo Fisher Scientific	Cat#PA5-22974; RRID:AB_11151839
Anti-EZH2 antibody	Cell Signaling	Cat#5246; RRID:AB_10694683
Anti-Biotin antibody	Jackson ImmunoResearch	Cat# 200-002-211, RRID:AB_2339006
Anti-Biotin antibody	Vector Laboratories	Cat# SP-3000, RRID:AB_2336111
Anti-CD44 (1D10) antibody	DSHB	Cat# 1D10; RRID: AB_2244424
Anti-Histone H3, Trimethyl (Lys27) (C36B11) Antibody	Cell Signaling Technology	Cat# 9733, RRID:AB_2616029
Anti-GAPDH antibody	Invitrogen	Cat# PA1-997; RRID:AB_2107311
Anti-CD68 antibody	BioLegend	Cat# 137012; RRID:AB_2074846
Anti-YAP1 antibody	Thermo Fisher Scientific	Cat# 13584-1-AP; RRID:AB_2218915
Alex Fluor 488 – conjugated AffiniPure goat anti-mouse IgG	Jackson ImmunoResearch	Cat# 115545003; RRID:AB_2338840
Alex Fluor 488 – conjugated AffiniPure goat anti-rabbit IgG	Jackson ImmunoResearch	Cat# 111545003; RRID:AB_2338046
Alex Fluor Rhodamine (TRITC) – conjugated goat anti-mouse IgG	Jackson ImmunoResearch	Cat# 115025003; RRID:AB_2338478
Alex Fluor Rhodamine (TRITC) – conjugated goat anti-rabbit IgG	Jackson ImmunoResearch	Cat# 111025003; RRID:AB_2337926
HRP goat anti-rabbit	BioRad	Cat# 1706515; RRID:AB_11125142
HRP goat anti-mouse	BioRad	Cat# 1706516; RRID: AB_11125547
<b>Biological samples</b>		
Pediatric patient-derived anterior lens capsule	Wills Eye Hospital	<a href="https://www.willseye.org/research-2/">https://www.willseye.org/research-2/</a>
<b>Chemicals, peptides, and recombinant proteins</b>		
Recombinant human TGF-beta 1 protein (240-B)	R&D Systems	Cat# 240-B-002/CF, GenPept: P01137
GSK-J4 inhibitor	Millipore Sigma	Cat# SML0701, CAS: 1373423-53-0
Thymidine	Millipore Sigma	Cat# T1895, CAS: 50-89-5
EdU (5-ethynyl-2'-deoxyuridine)	Invitrogen	Cat# A1004
DMSO	Thermo Fisher Scientific	Cat# AAA1328036
DAPI	BioLegend	Cat#422801
<b>Critical commercial assays</b>		
RNeasy Mini Kit	Qiagen	Cat# 74104
NucleoSpin RNA/Protein, Mini Kit	Macherey-Nagel	Cat# 740933
High Pure RNA Isolation Kit	Roche Life Sciences	Cat# 11828665001

(Continued on next page)

### Continued

REAGENT or RESOURCE	SOURCE	IDENTIFIER
iScript Reverse Transcription Superscript	Bio-Rad	Cat# 1708840
Super-Script IV First-Strand Synthesis System	Invitrogen	Cat# 18091050
Sso Fast EvaGreen Superscript	Bio-Rad	Cat# 172-5200
PowerUp SYBR Green Master Mix	Applied Biosystems	Cat# A25741
Masson's Trichrome Stain Kit	Polysciences	Cat# 25088
Click-iT EdU Cell Proliferation Kit for Imaging, Alex Fluor 499 dye	Invitrogen	Cat# C10337

### Deposited data

Raw and analyzed data	This paper	GEO: GSE213480
-----------------------	------------	----------------

### Experimental models: Cell lines

Human: pulmonary fibroblasts	ScienCell Research Laboratories	Cat# 3300
------------------------------	---------------------------------	-----------

### Experimental models: Organisms/strains

<i>Gallus Gallus</i>	Charles River	N/A
<i>Gallus Gallus</i>	Poultry Futures	N/A
Mouse: C57BL/6J	The Jackson Laboratory	RRID:IMSR_JAX:000664

### Oligonucleotides

For primers see Table S2	This paper	N/A
--------------------------	------------	-----

### Software and algorithms

ImageJ	Schneider et al. <sup>7</sup>	<a href="https://imagej.nih.gov/ij/">https://imagej.nih.gov/ij/</a>
GraphPad Prism	GraphPad Software	<a href="https://www.graphpad.com/scientific-software/prism/">https://www.graphpad.com/scientific-software/prism/</a>
NIS-Elements Basic Research	Nikon	<a href="https://www.microscope.healthcare.nikon.com/en_EU/products/software/nis-elements">https://www.microscope.healthcare.nikon.com/en_EU/products/software/nis-elements</a>
ZEN Microscopy Software	ZEISS	<a href="https://www.zeiss.com/microscopy/en/products/software/zeiss-zen.html">https://www.zeiss.com/microscopy/en/products/software/zeiss-zen.html</a>

## RESOURCE AVAILABILITY

### Lead contact

Further information and requests for resources and reagents should be directed to and will be fulfilled by the lead contact, Janice L. Walker ([Janice.Walker@jefferson.edu](mailto:Janice.Walker@jefferson.edu)).

### Materials availability

All materials generated in this study are available upon request from the [lead contact](#), Janice L. Walker.

### Data and code availability

- The RNA-sequencing data has been deposited at Gene Expression Omnibus (GEO) and is publically available as of the date of publication. The accession number is GSE213480. All other original data reported in this paper will be shared by the [lead contact](#) upon request.
- This paper does not report original code.
- Any additional information required to reanalyze the data reported in this paper is available from the [lead contact](#) upon request.

## EXPERIMENTAL MODEL AND STUDY PARTICIPANT DETAILS

### Ex vivo post cataract surgery cultures

Chicken embryonated eggs were procured from Charles River (Wilmington, MA, USA) and Poultry Futures (Lititz, PA, USA). Ex vivo post-cataract surgery cultures were prepared on lenses isolated from embryonic day 14/15 chicken embryos of randomized sex. Mock cataract surgery was performed on isolated lenses

as previously described.<sup>38</sup> Explants were cultured in complete media containing Media 199 (Thermo Fisher Scientific, Waltham, MA, USA), 1% penicillin/streptomycin (Mediatech-Cellgro, Manassas, VA, USA), 1% l-glutamine (Mediatech-Cellgro, Manassas, VA, USA) with 10% fetal calf serum (Thermo Fisher Scientific, Waltham, MA, USA). Inhibitor treatments were added at indicated times to culture media. All studies using chicken embryos comply with the Association for Research in Vision and Ophthalmology Statement for the Use of Animals in Ophthalmic and Vision Research and all procedures were conducted in accordance with Thomas Jefferson University Institutional Animal Care and Use Committee.

### Pediatric human lens explants

Pediatric human lens explant model was developed using tissue from patients undergoing manual anterior curvilinear capsulorhexis (all  $\geq 4$  years old) at Wills Eye Hospital (Philadelphia, PA, USA). Other identifying information of patients including ethnicity, sex, and gender were not disclosed. Explants consisting of anterior lens capsule and associated cells were torn into two samples. Using Corning Cell-Tak Cell and Tissue Adhesive (Millipore Sigma, St. Louis, MO, USA) each sample was attached to separate 35 mm tissue culture dishes. Explants were cultured in complete media as described above for the chicken embryo model and were maintained in a humidified incubator at 37°C in 5% CO<sub>2</sub>. The studies with human pediatric samples were Institutional Review Board (IRB) approved through Will's Eye Hospital (IRB #13–365). Pediatric patients undergoing cataract surgery were recruited consecutively through Wills Eye Hospital (Philadelphia, PA, USA). Informed consent was obtained after the nature of the study was explained.

### Primary human lung fibroblasts

Primary HLF were purchased from ScienCell Research Laboratories, Carlsbad, CA, USA. The sex of primary HLFs is not reported by ScienCell Research Laboratories. Primary HLFs were authenticated by ScienCell Research Laboratories which stated cells were characterized by immunofluorescence using an antibody specific to fibronectin and tested negative for HIV-1, HBV, HCV, mycoplasma, bacteria, yeast, and fungi. HLFs were cultured in DMEM supplemented with 10% FBS, L-glutamine, ascorbic acid 2-phosphate, penicillin/streptomycin and grown in a humidified incubator at 37°C in 5% CO<sub>2</sub>. Fibroblasts were stimulated with 5 ng/ml TGF- $\beta$ 1 (R&D Systems, Minneapolis, MN) to induce transition to myofibroblasts.

### Bleomycin mouse model

Bleomycin (0.05U/kg) was instilled into the lungs to 15 8-week-old male C57BL6/J mice (Jackson Laboratory, Bar Harbor, ME) using the “tongue-pull” methods.<sup>59</sup> Seven days later, subdermal osmotic pumps were implanted (Alzet No. 1004) containing either vehicle control (DMSO) or GSK-J4 dissolved in DMSO released at a rate of 3 mg/kg/day. Five mice that did not receive bleomycin served as controls. At twenty-one days post-instillation of bleomycin and fourteen days post-implantation of pumps, mice were sacrificed. Lungs from three mice were inflated with 4% buffered formalin to preserve lung structure. Lung lobes from remaining mice were isolated and processed for isolation of total RNA and for measurement of hydroxyproline content. All procedures using mice were conducted in accordance with Thomas Jefferson University Institutional Animal Care and Use Committee.

## METHOD DETAILS

### Immunofluorescence staining and confocal imaging

Ex vivo mock cataract surgery cultures were prepared in 35 mm dishes and fixed at room temperature with 4% paraformaldehyde in PBS for 15min. Cultures were then washed with DPBS, permeabilized with 0.25% Triton X-100 in DPBS for 10min, and incubated in block buffer made of 0.5% goat/donkey serum in DPBS for 30 min. After blocking buffer incubation, cultures were incubated in primary antibody diluted in 0.1% Tween 20 in DPBS for 30 min at 37°C. Primary incubation was followed by 30 min incubation in secondary antibody diluted in 0.1% Tween 20. Primary antibodies for the chick lens study used included:  $\alpha$ SMA (ab2547, Sigma Aldrich, St. Louis, MO, USA or Abcam, Cambridge, MA, USA), MRTF-A (ab49311, Abcam, Cambridge, UK), FN-EDA (IST-9, Santa Cruz Biotechnology, Dallas, Texas, USA), YAP1 (13584-1-AP, ThermoFisher Scientific, Waltham, MA, USA). The following primary antibodies were obtained from Developmental Studies Hybridoma Bank, created by the NICHD of the NIH: CD44 (1D10, DSHB, Iowa City, Iowa, USA), FN-EDA (IST-9, Santa Cruz Biotechnology, Dallas, Texas, USA), Collagen, Type I pro-peptide (SPI.D8, DSHB, Iowa City, Iowa, USA) To detect F-actin and nuclei respectively, cultures were counterstained with fluorescent conjugated Phalloidin (ThermoFisher Scientific, Waltham, MA, USA) and/or DAPI (Biolegend, San Diego, CA). Fluorescently labeled samples were imaged using a Zeiss LSM800 confocal microscope.

For confocal images, confocal z-stacks with 0.33  $\mu\text{m}$  optical sections were collected and analyzed using Zen software. Fluorescence intensity of images were quantified using ImageJ software.

### Hydroxyproline

Entire right superior lobes from three mice were weighed and completely hydrolyzed in 6N HCl overnight at 110°C. HCl was evaporated and hydrolyzed samples were resuspended in 1 mL dH<sub>2</sub>O and stored at 4°C. Hydroxyproline in the hydrolyzate was oxidized by chloramine T, the resulting chromagen was coupled with Ehrlich's aldehyde in a strong perchloric acid solution and the absorbance of the solution measured at 557 nm. The total content of hydroxyproline was determined from a standard curve prepared by dissolving hydroxyproline in distilled H<sub>2</sub>O and calculated based on the initial volume of each hydrolyzate sample. The hydroxyproline content was expressed as total  $\mu\text{g}$  hydroxyproline per mg of the lung lobe hydrolyzed.

### Masson's trichrome

Lungs inflated with 4% buffered formalin were dehydrated, embedded in paraffin, and sectioned. Sections were deparaffinized in graded ethanol series and stained using the Masson's Trichrome Staining Kit (PolySciences, Warrington, PA, USA). Photographs were taken with a Zeiss light microscope equipped with a Nikon digital camera.

### Western blot analysis

Samples were lysed in RIPA buffer (5 mM EDTA, 150 mM NaCl, 1% NP40, 1% sodium deoxycholate, 1% SDS, 50 mM Tris-HCl, pH 7.4). Protein concentrations were determined with Pierce BCA assay. Proteins were immunoblotted using primary antibodies and secondary antibodies listed in the [key resources table](#). ECL reagents were used for detection on ProteinSimple Fluorchem M system. Protein Simple software was used to quantify mean intensity of proteins.

### Chromatin assembly assay and analysis

Ex vivo post-cataract surgery cultures and primary HLF were pulse-labeled with 5  $\mu\text{M}$  EdU for 30 or 20min, respectively, and followed with a chase where indicated before being fixed at room temperature with 4% paraformaldehyde in PBS for 15min, washed with PBS, and permeabilized with 0.3% Triton for 15min. Click-iT reaction with biotin-azide was performed for 30min. The PLA reactions (Sigma Aldrich, St. Louis, MO) between the anti-biotin antibody and antibodies to other proteins were performed according to manufacturer's instruction ([key resources table](#): Duolink): after primary antibody incubation, secondary antibodies conjugated to oligonucleotides (Duolink PLA probes PLUS and MINUS) were incubated for 1h and the ligase and two oligonucleotides that hybridize to PLA probes if in close proximity were added. Then, PCR amplification solution containing the fluorescently labeled oligonucleotides that hybridize was added. Following PLA, cells were immunostained with anti-biotin Alexa Fluor 488 antibody to control the specificity of CAA. The results of CAA experiments shown in the figures were quantified by counting the number of PLA signals per EdU-labeled nuclei in each independent experiment. Antibodies used for CAA: UTX (33510, Cell Signaling, Danvers, MA, USA), H3K27me3 (Cell Signaling, MA, USA), MRTF-A (sc-32909, Santa Cruz, Dallas, TX, USA), YAP1 (13584-1-AP, ThermoFisher Scientific, Waltham, MA, USA), mouse anti-biotin (Jackson ImmunoResearch, West Grove, PA), goat anti-biotin (Vector Laboratories, Burlingame, CA). CAA images were captured with a Nikon Eclipse Ni microscope and analyzed using NIS elements software. Images were taken at single optical sections and merged using NIS elements software to obtain one image.

### Treatment with thymidine

To block DNA replication, the ex vivo post-cataract surgery cultures and primary HLF were labeled with EdU for 30min and treated with 5 mM or 2 mM thymidine (T1895, Sigma Aldrich, St. Louis, MO, USA), respectively, for 24h. To release into S phase, thymidine was removed by washing, and cells were grown for 0h and 4h and fixed. To assess the binding of MRTF-A CAA was performed with antibodies against biotin (to detect EdU-labeled DNA) and MRTF-A. To ensure efficacy of the thymidine block and release, cells were labeled for 30 min with 5  $\mu\text{M}$  EdU after 24h thymidine treatment or 24h thymidine treatment and 4h release. To determine whether DNA replication is required for the fibrotic phenotype in the lens, ex vivo post-cataract surgery cultures were treated with 5 mM thymidine from Day 1 through Day 3 and analyzed by IF and/or WB analysis. Cells were fixed with 4% paraformaldehyde and Click-iT reaction was performed using Click-iT EdU Cell Proliferation Kit for Imaging, Alexa Fluor 488 dye.

### Proliferation

To assess replicative potential of leader cells cultures were labeled with EdU were labeled for 1h or 30 min. Click-iT reactions were performed using Click-iT EdU Cell Proliferation Kit for Imaging, Alexa Flour 488 dye according to manufacturer's directions.

### Inhibition of H3K27 KDMs by GSK-J4

To inhibit H3K27me3 KDM activity in lens fibrosis models, *ex vivo* post-cataract surgery cultures and human lens pediatric cultures were treated with 7.5  $\mu$ M or 2.5  $\mu$ M GSK-J4 (Sigma Aldrich, St. Louis, MO, USA), respectively, dissolved in DMSO. Post-cataract surgery explants were treated +/- GSK-J4 at 20h post-injury and grown in the presence of this treatment for 8h or until day 3 post-injury. The vehicle DMSO was added in control experiments. Human pediatric lens explants were given 48h to recover in culture and then were treated with 7.5  $\mu$ M GSK-J4 dissolved in DMSO or appropriate DMSO vehicle control. Cultures were treated continuously for 6 days before being fixed with 4% paraformaldehyde and processed for analysis. To inhibit H3K27me3 KDM activity in lung fibrosis models, primary HLF were pretreated with 2.5  $\mu$ M GSK-J4 for 12h prior to induction with 5 ng/ml TGF- $\beta$ 1 for 0h and 48h. DMSO without GSK-J4 was added in control wells. Mice were treated with bleomycin for 7 days, given pumps containing 3 mg/kg/day GSK-J4 on day 8 and were harvested on day 22 (14 days post-implantation). Control mice without bleomycin or GSK-J4 were harvested at the same time. All experimental samples were processed for CAA (MRTF-A and H3K27me3), extracted for western blot analysis, fixed for immunofluorescence studies, Masson's Trichrome, hydroxyproline, or collected for gene expression analysis.

### RNA-seq analysis

Total RNA from 3 individual experiments were isolated directly from *ex vivo* mock cataract surgery cultures treated with GSK-J4 or vehicle control (DMSO) on day 3 post-injury using Qiagen RNeasy Mini Kit. A total of 12 GSK-J4 treated lenses (4 lenses per experiment) and 12 DMSO (4 lenses per experiment) treated lenses were used for library preparation for transcriptome sequencing and analysis performed by Novogene Co., LTD (Beijing, China). An adjusted p-value <0.05 and absolute foldchange of 2 were set as the threshold for significant DEGs. GO and KEGG enrichment analysis of DEGs were then performed.

### Chromatin immunoprecipitation

ChIP was performed with MRTF-A antibody and values represent means of three independent experiments. For ChIP assay, HLF were grown on 100 mm dishes and cross-linked for 10 min in 1% formaldehyde. The lenses were also cross-linked for 10 min in 1% formaldehyde. Cells or lenses were lysed and homogenized in RIPA buffer (1% Triton X-100, 0.1% sodium deoxycholate, 0.1% SDS, 0.15 M NaCl, 10 mM Tris-HCl, pH 8.0, 1 mM EDTA, pH 8.0 with protease inhibitor) following sonication to shear chromatin to an average length of about 200–500 bp. Aliquots of chromatin were incubated overnight with 10 $\mu$ g of MRTFA antibody (Santa Cruz Biotechnology) or 10  $\mu$ g of rabbit IgG. The protein G magnetic beads were added for 1 h. Beads were sequentially washed for 3–5 min 2 times with RIPA buffer, followed by washes with LiCl wash buffer (0.25 M LiCl, 1% NP40, 1% deoxycholate, 1 mM EDTA, 10 mM Tris-HCl pH 8.1) and then twice with TE (10 mM Tris-HCl pH, 8.0, 1 mM EDTA). Immunoprecipitated material was removed by incubation in elution buffer (1% SDS, 0.1 M NaHCO<sub>3</sub>) for 30 min. Samples were incubated overnight at 65°C to reverse crosslinking and treated with proteinase K for 2 h at 45°C. DNA was purified by phenol/chloroform extraction and precipitated with ethanol. All PCR reactions were performed with an Applied Biosystems StepOne Real-Time PCR system. The sequences for primers for ChIP analysis for human and chicken ACTA2 and COL1A1 are located within [Table S2](#).

### Wound healing

For wound healing studies, *ex vivo* post-cataract surgery cultures were treated with GSK-J4 immediately at the time of injury and each subsequent day until wound closure. The wound area was imaged using an AZ100 Nikon microscope. The wound area was measured by NIS elements software to calculate the percent of wound closure.

### Gene expression analysis by RT-qPCR

Total RNA was isolated directly from *ex vivo* mock cataract surgery cultures day 3 post-injury with or without GSK-J4 treatment using Qiagen RNeasy Mini Kit and from left lobes of three mice using Macherev-Nagel Nucleospin RNA/Protein Kit (TakaraBio #740933). Total RNA from Human primary lung fibroblasts was

isolated using High Pure RNA isolation Kit (Roche Life Science, Penzberg, Germany). cDNA was synthesized using iScript Reverse Transcription Supermix (1708840, BIO-RAD, Hercules, CA, USA) or SuperScript IV First Strand cDNA Synthesis Kit (Invitrogen, Waltham, MA). After reverse transcription was complete, real-time PCR was carried out on a BIO-RAD CFX96 Real Time System or QuantStudio 12k Flex system (ThermoFisher) using either Sso Fast EvaGreen Supermix (172–5200, BIO-RAD, Hercules, CA, USA) or 2x Power SYBER green PCR master mix (4309155, Thermo Fisher, Waltham, MA, USA). *GAPDH* or  $\beta$ -*Actin* was used as an internal control. PCR analyses were conducted in triplicate for each sample. The sequences for primers for mouse and chicken pro-fibrotic genes and markers of the pro- and anti-inflammatory immune response are located in [Table S2](#).

## QUANTIFICATION AND STATISTICAL ANALYSIS

Statistical analysis was performed using GraphPad Prism software. For all experiments, data are expressed as average  $\pm$  standard error of mean (SEM). Statistical significance was calculated using unpaired t test or using one-way analysis of variance (ANOVA) with multiple comparisons. Results were considered significant when  $p < 0.05$ . Statistical analysis details of all experiments can be found in the corresponding figure legend and specific p values are stated with each figure reference in the results.